A Simulation Code for 3-Dimensional Non-Linear Incompressible Resistive MHD in a Periodic Cylinder
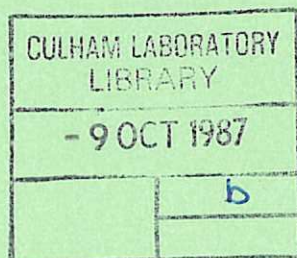
P. Kirby

UK ATOMIC ENERGY AUTHORITY

Culham Laboratory

A Simulation Code for 3-Dimensional Non-Linear Incompressible Resistive MHD in a Periodic Cylinder

P. Kirby

Culham Laboratory, Abingdon, Oxfordshire, OX14 3DB, U.K.

(Euratom/UKAEA Fusion Association)

Abstract

This paper describes the construction of a computer code that models 3-dimensional non-linear, resistive, incompressible MHD in a periodic cylinder and presents results from typical calculations.

February, 1987.

1.Introduction

This paper describes the construction and use of a numerical simulation
code ('MERCURY') that models 3-dimensional, non-linear, resistive,
incompressible magneto-hydrodynamics (MHD) in a periodic cylinder. Its
purpose is to discuss the considerations of algorithms, implementation and
optimization involved in such a code, to point out the strengths and
weaknesses of the choices adopted here, and to indicate the scope of the
calculations that may be performed.

The context of the present work is that of Controlled Thermonuclear Fusion
research, in particular the study of processes that occur in laboratory
devices for plasma confinement using magnetic fields in toroidal geometry
[1]. The principal application [2] of the code has been to the classic
problem of the spontaneous reversal of the magnetic field in the Reversed
Field Pinch [3]. The code has also been used [4] to investigate certain
aspects of internal instabilities (sawtooth oscillations) in the JET
tokamak [5].

A fundamental problem for such numerical calculations is the enormous
range of time scales (10^{-11}s - 1s) and length scales (10^{-6}m - 1m) involved
in a real plasma. This puts an all-inclusive simulation beyond
computation and forces the use of a model plasma, simplified appropriately
for the phenomenon under investigation. In particular, for macroscopic
motion it is conventional to adopt the simplest description (the MHD
model), in which the plasma is regarded as a single electrically

conducting fluid. Although this simplification is often hard to justify formally, it is widely accepted as a convenient basis for discussion [6].

The main feature of the present MHD model is the further assumption of incompressibility. The reason for this choice was not directly that of simplifying the numerical problem, but rather that of providing a particularly clean physics system with which to discuss the field reversal problem, under the assumption that it is a gross electromechanical effect, not essentially altered by detailed plasma properties. Insofar as incompressible codes do give field reversal, this hypothesis appears to be justified, at least for the present purpose of gaining physical insight. Further general justification is the fact that many plasma instabilities are essentially incompressible.

It should be noted, however, that there are certainly detailed differences between incompressible and compressible MHD models. These have appeared in comparison calculations [7] of field reversal (a paper open to mis-interpretation in the view of the present author) and in calculations [8] of non-linear m = 1 tearing modes, in which the incompressible model shows saturation but the compressible model is known to reconnect completely.

The assumption of incompressibility leads to a simplification of the numerical problem because there is then no separate equation for the pressure. Moreover, magnetosonic waves are completely excluded from the system, thereby eliminating the corresponding numerical timestep restriction, most significantly that from fast magnetosonic waves propagating in the poloidal direction near the origin of a polar mesh.

Formerly, such restrictions were severe and forced compressible codes to use significantly shorter timesteps than incompressible ones, which therefore had a considerable operational advantage.

This picture has been completely changed by the recent introduction [9, 10, 11, 12] of the semi-implicit method [13] from meteorology into MHD simulation. This practical technique now provides unconditional numerical stability of magnetosonic and Alfvén waves and allows the timestep to be determined solely by consideration of accuracy. It may therefore be expected that future MHD codes for plasma simulation will be compressible and semi-implicit. Since the current version of the present code does not use the semi-implicit method, it will not be discussed further in this paper.

A principal feature of the numerical approach is the use of a spectral method in θ and z, implemented using Fast Fourier Transforms (FFTs). This means that all harmonics are included in the calculation, up to the inevitable limit imposed by the finite mesh. This is in line with the application e.g. [14] of spectral methods in hydrodynamics. The use of FFTs is then fundamental since the computational cost is $O(N \log_2 N)$ rather than $O(N^2)$ for the direct interaction of N harmonics. FFTs have been used previously in MHD calculations in [15].

It should be noted that this approach is different from that widely used in plasma MHD simulations, namely the direct interaction of particular Fourier harmonics ('modes') selected a-priori from an ordering tree. This has arisen because it is often physically meaningful to study individual modes, and this can be done simply by carrying only the required mode and

those that can be generated from it by the (usually quadratic) non-linearities. The weakness of this approach is the difficulty of extending it to the general case. For, if all modes are included, the computational cost may become prohibitive. Conversely, if some modes are excluded to reduce cost, the calculation has been biased from the outset.

Many 3D non-linear codes have been written over the years, starting with the TRINITY code [16] of Roberts and Boris in 1969, and it is not the intention to produce a complete list here. A review of such codes to 1981 may be found in [17]. Notable amongst these is the NONLIN code of Sykes and Wesson, used to simulate field reversal [18] and tokamak sawtooth oscillations [19]. Examples of later work may be found in [7, 10, 20, 21, 22, 23, 24]. Apart from the use of FFTs, the present approach is somewhat similar to that of Aydemir and Barnes [20].

A strategic weakness of most of these codes, and the present one, is the use of straight geometry on grounds of simplicity, instead of correct toroidal geometry. This approximation may be acceptable for the simulation of pinches (q < 1), but is probably less so for tokamaks (q > 1), depending on circumstances. Non-linear codes using toroidal geometry e.g. [23] are however becoming available.

The contents of the paper are as follows:

Section 1:   Introduction

Section 2:   Basic equations

Section 3:   Numerical methods

Section 4:   Diagnostic facilities

Section 5:   Program optimization and testing

Section 6:   Typical simulations

- 4 -

2. Basic equations

The basic equations are those of single-fluid, scalar pressure, resistive MHD with the assumption of constant uniform density and isotropic resistivity and viscosity. They may be written in non-dimensional form

$$\frac{\partial \underline{v}}{\partial t} + (\underline{v} \cdot \nabla)\underline{v} = - \nabla p + \underline{j} \times \underline{B} + \nu \nabla^2 \underline{v} \qquad (1)$$

$$\underline{E} + \underline{v} \times \underline{B} = \frac{\eta}{S} \underline{j} \qquad (2)$$

$$\nabla \times \underline{E} = - \frac{\partial \underline{B}}{\partial t} \qquad (3)$$

$$\nabla \times \underline{B} = \underline{j}$$

$$\rho = 1$$

$$\nabla \cdot \underline{v} = 0.$$

Elimination of $\underline{E}$ and $\underline{j}$ from (2) gives

$$\frac{\partial \underline{B}}{\partial t} = \nabla \times (\underline{v} \times \underline{B} - \frac{\eta}{S} \nabla \times \underline{B}) . \qquad (4)$$

Here, dimensional quantities have each been expressed as the product of a dimensional characteristic value and a dimensionless variable.

The characteristic values for length (x_0), magnetic field (B_0), resistivity (η_0), and density (ρ_0) are regarded as primary values, specified as input in S.I. units. The derived characteristic values are then

current density: $\qquad j_0 = B_0/(x_0\mu_0)$

electric field: $\qquad E_0 = x_0 B_0/t_0$

velocity: $\qquad v_0 = B_0/(\mu_0\rho_0)^{1/2}$

time: $\qquad t_0 = x_0/v_0$

pressure: $\qquad p_0 = \rho_0 v_0{}^2$

viscosity: $\qquad \nu_0 = x_0{}^2/t_0$

resistive timescale: $\quad t_R = \mu_0 x_0{}^2/\eta_0$

Lundquist number: $\quad S = t_R/t_0$.

Note that the code runs on the Alfvén timescale. In this model, the resistivity η is not a calculable quantity and must be specified arbitrarily. Provision for a radial dependence $\eta = \eta(r)$ has been included for compatibility with experimental conditions. The use of an isotropic resistivity (chosen on the grounds of simplicity) rather than the more correct anisotropic form $\eta_\perp = 2\eta_\parallel$ means that the paramagnetic effect [25]

is absent from the model. This may make field reversal harder to obtain than it would otherwise be.

Equations (1) and (4) are the basic equations for the present calculations. There is no separate equation for the pressure since it is fixed by the condition $\nabla \cdot \underline{v} = 0$ and is determined by taking the divergence of the momentum equation (1). Although viscosity is probably physically unimportant for present purposes, as discussed below it has been included to ensure the non-linear numerical stability of the code.

Even though the MHD equations are known to give only a very simplified model of a real plasma; their use on the field reversal problem seems eminently justified. For, given the robust nature of this remarkable phenomenon, it is very likely that even a simple model will help clarify the mechanism in a real experiment.

3.   Numerical methods

This section contains a description of the numerical techniques used to advance equations (1) and (4).

As stated above, a feature of the present approach is the use of a spectral method and FFTs in the periodic directions θ and z. The use of spectral representations is motivated by the results of Orszag in hydrodynamics calculations [26] which suggested that for smooth flows a reduction of 1/2 in computational effort could be obtained, compared with finite differences, for the same accuracy. Comparisons for MHD seem to confirm this view [15].

The initial approach adopted in the code was pseudospectral. In this method, equivalent to a truncated series expansion with a collocation approximation, the emphasis is on the grid point representation and the Fourier transform is viewed as an accurate means of computing derivatives by transforming to k-space, multiplying by ik and then transforming back to grid point.

The disadvantage of the method is its susceptibility to aliasing error [27], in which unresolvably short wavelengths, generated by non-linear terms, re-appear erroneously as long wavelengths. In the present low dissipation MHD simulations, these errors can lead to the rapid onset of numerical instability.

As a result of this experience, the spectral method was adopted. In this method, equivalent to a truncated series expansion with a Galerkin approximation, the discrete equations are obtained by minimizing the mean square truncation error. An important consequence of this approach is that the aliasing effect is excluded. The method has been implemented by proceeding as for the pseudospectral method, but then setting to zero at every timestep the top 1/3 of the available Fourier harmonics.

Conventional second-order finite differences are used in the radial direction for reasons of simplicity. Since the flexibility of a variably spaced mesh is largely unusable in a general simulation, an equally spaced mesh has been used from the outset. As described below, the aliasing error associated with the radial finite differences can lead to the rapid failure of non-linear simulations due to the growth of an explosive

numerical instability. The viscosity term is needed for its suppression in the present case.

This behaviour represents a considerable deficiency of elementary finite difference methods for low dissipation MHD simulations and points to the importance of non-linear numerical schemes that conserve quadratic invariants identically. This has traditionally been ignored in plasma MHD codes, despite its long recognition in other fields [28].

The sections below contain a discussion of the following topics:

1. coordinate system

2. time advancement scheme

3. linear numerical stability analysis

4. Fourier representation and spatial derivatives in θ and z

5. radial mesh and differencing in r

6. regularity conditions at the origin

7. boundary conditions

8. solution of the pressure equation

9. implicit treatment of resistivity

10. de-aliasing in θ and z

11. radial aliasing and additional velocity smoothing

3.1   The coordinate system

The calculation is performed in a straight periodic cylinder using cylindrical polar coordinates $\{r, \theta, z\}$. By choice of normalization, $r = 1$ is the wall. The poloidal and axial ('toroidal') mode numbers are

denoted by m and n respectively. L is the periodic length in the z direction. The permitted axial wave-numbers k are therefore given by $k_n = (2\pi/L)n$. $L/2\pi$ is the equivalent toroidal major radius.

The primitive variables (3 components each of $\underline{B}$ and $\underline{v}$) are stored as functions of $\{r, \theta, z\}$.

3.2   The time advancement scheme

There are 4 specific considerations in choosing a time advancement scheme for the present problem: complexity of implementation; maintenance of $\nabla \cdot \underline{B} = 0$ and $\nabla \cdot \underline{v} = 0$; numerical stability at large S, i.e. small physical dissipation; numerical stability at the origin of the polar mesh.

Considerations of complexity clearly favour explicit methods and implicit methods that produce only linear tridiagonal equations. Although fully implicit, non-linear, 3D MHD calculations have been attempted [29], this difficult approach does not appear to hold any obvious advantage, especially with the availability of the semi-implicit method.

The requirement of solenoidal $\underline{v}$ may be met by the use of the standard MAC method [30] for incompressible flow, in which the pressure is corrected at each timestep. The requirement of solenoidal $\underline{B}$ may be met either by the use of the vector potential or, as in the present code, by the use of numerical operators such that $\nabla \cdot \nabla \times \underline{B} \equiv 0$. The need to enforce $\nabla \cdot \underline{B} = 0$ by some means is well illustrated by the recognized [31] failure of MHD codes in astrophysics in which this is often ignored.

The presence of only small physical dissipation means that the hyperbolic parts of the system must be made intrinsically linearly numerically stable. For reasons of simplicity and familiarity, the choice of time advancement for the present code has been deliberately limited to traditional work-horse methods [32]. Accordingly, the code achieves this stability by use of an elementary 2-step forward-time scheme [33]. A property of the forward-time advance is the introduction of numerical dissipation. For schemes requiring conservation properties, a centred-time advance may therefore be more appropriate.

The need for numerical stability at the origin of the polar mesh forces an implicit treatment of resistivity. This follows from the familiar timestep restrictions for explicit schemes, namely

$$\frac{\Delta t}{S \Delta x^2} \leqslant 1 \quad \text{and} \quad \frac{v \Delta t}{\Delta x} \leqslant 1 \ .$$

Here v is a typical Alfvén velocity and Δx a typical mesh spacing. Near the origin of a polar mesh, $\Delta x \sim \Delta r \Delta \theta$, $v_\theta \sim B_\theta \sim \Delta r$, so that the ratio of the parabolic timestep limit to the hyperbolic one is $S/(N_r^2 N_\theta)$. This would be significantly less than unity for many cases of interest and would present a restriction for practical use.

The same consideration applies to the viscosity term. In the current version of the code, this term has in fact been treated explicitly, on the assumption that the magnitude of the viscosity required will be small. This is a weakness of the code (indicative of its development route) that will be amended in a later version.

The basic equations (1) and (4) are advanced in time according to the 2-step scheme as follows:

$$\underline{B}^* = \underline{B}^n + \Delta t \; \nabla \times \left(\underline{v}^n \times \underline{B}^n - \frac{\eta}{S} \nabla \times \underline{B}^* \right) \tag{5}$$

$$\underline{v}^* = \underline{v}^n + \Delta t \left(-\underline{v}^n \cdot \nabla \underline{v}^n + \underline{j}^n \times \underline{B}^n - \nabla p^* + \nu \nabla^2 \underline{v}^n \right)$$

$$\underline{B}^{n+1} = \underline{B}^n + \Delta t \; \nabla \times \left(\underline{v}^* \times \underline{B}^* - \frac{\eta}{S} \nabla \times \underline{B}^* \right) \tag{6}$$

$$\underline{v}^{n+1} = \underline{v}^n + \Delta t \left(-\underline{v}^* \cdot \nabla \underline{v}^* + \underline{j}^* \times \underline{B}^* - \nabla p^{n+1} + \nu \nabla^2 \underline{v}^* \right)$$

A feature of this scheme is that resistivity need be treated implicitly only in the first step.

The pressure is obtained at each step by taking the divergence of the velocity equation and applying $\nabla \cdot \underline{v} = 0$ at the new time but not assuming this for the old $\underline{v}$ (this is the essence of the MAC approach). The resulting Poisson equation may be written

$$\nabla^2 p^* = \frac{1}{\Delta t} \nabla \cdot \underline{v}^n + \nabla \cdot \left(-\underline{v}^n \cdot \nabla \underline{v}^n + \underline{j}^n \times \underline{B}^n + \nu \nabla^2 \underline{v}^n \right) \tag{7}$$

and similarly for p^{n+1}. The consistent implementation of this equation leads to the use of a staggered radial mesh.

3.3   Linear numerical stability analysis

This section contains a discussion of the linear numerical stability of (5), (6) and related schemes. For tractability, the analysis is confined to slab geometry. Furthermore, for simplicity, no account is taken of the staggered radial mesh used in practice (section 3.5). Since numerical stability properties are generic and generally independent of precise details, such simplifications are not unreasonable for present purposes.

As stated above, the 2-step scheme is used to stabilize the hyperbolic part of the equation; considering the 1D advection equation

$$\frac{\partial u}{\partial t} + v \frac{\partial u}{\partial x} = 0$$

as a simple example, the forward-time, centred-space scheme

$$u_j^{n+1} = u_j^n - \frac{c}{2} (u_{j+1}^n - u_{j-1}^n)$$

has dispersion relation

$$\exp(-i\omega\Delta t) = 1 - ic \sin k\Delta x$$

(substituting $u_j^n \sim \exp i(kj\Delta x - n\omega\Delta t)$ with $c \equiv v\Delta t/\Delta x$) and is therefore unconditionally unstable; conversely the 2-step scheme

$$u_j^* = u_j^n - \frac{c}{2} (u_{j+1}^n - u_{j-1}^n)$$

$$u_j^{n+1} = u_j^n - \frac{c}{2}(u_{j+1}^* - u_{j-1}^*)$$

has dispersion relation

$$\exp(-i\omega\Delta t) = 1 - c^2 \sin^2 k\Delta x - ic \sin k\Delta x$$

and is therefore numerically stable for $c^2 \leqslant 1$. This scheme ('Brailovskaya-time, centred-space', BTCS) is analogous to the treatment of the radial direction in (5), (6).

Before proceeding with the full stability analysis, it is a useful reminder of the limitations of the numerical scheme to apply it to a simple analytic test case. The performance of the 2-step scheme on the advection of a Gaussian pulse is compared in Fig.1 with that of the conventional forward-time, upwind-space scheme (FTUS),

$$u_j^{n+1} = u_j^n - c(u_j^n - u_{j-1}^n) \qquad (c > 0)$$

the fully implicit forward-time scheme (IMPL),

$$u_j^{n+1} = u_j^n - \frac{c}{2}(u_{j+1}^{n+1} - u_{j-1}^{n+1})$$

the Lax-Wendroff scheme (LAXW),

$$u_j^{n+1} = u_{j-1}^n \frac{c}{2}(c+1) + u_j^n(1-c^2) + u_{j+1}^n \frac{c}{2}(c-1)$$

the centred-time, centred-space scheme (CTCS),

$$u_j^{n+1} = u_j^{n-1} - c(u_{j+1}^n - u_{j-1}^n)$$

and the Brailovskaya-time, spectral-space scheme (BTSS),

$$\tilde{u}^* = \tilde{u}^n - ikv\Delta t\, \tilde{u}^n$$

$$\tilde{u}^{n+1} = \tilde{u}^n - ikv\Delta t\, \tilde{u}^*$$

in which the $\tilde{u}$ are the Fourier coefficients of u. This scheme is
analogous to the treatment of the θ and z directions in (5), (6). These
results demonstrate that the centred-time schemes have less numerical
dissipation than the forward-time schemes, but can show greater over all
phase error. (For the case of BTSS, the entire error derives from the
time discretization. If a recognized ordinary differential equation
solver, such as Runge-Kutta, is then used for the time advance, remarkably
high accuracy may be achieved).

The MHD numerical stability analysis may be made by noting that in the
present mixed finite-difference, spectral representation, all quantities
have the form

$$\underline{B}(x_j) = \sum_{\underline{k}} \underline{\tilde{B}}(x_j)\, \exp\, i(k_y y + k_z z),$$

in which x is interpreted as the radial coordinate. Derivatives in y
and z are obtained by analytic differentiation, those in x by centred
finite differences. Upon substitution of

$$\underset{\sim}{\underline{B}}(x_j) \equiv \underline{B} \exp i(k_x x_j - \omega t),$$

the Fourier transformed versions of the numerical vector operators may be
written

$$\underset{\sim}{\tilde{\nabla}} \cdot \underline{B} = i\underline{\kappa} \cdot \underset{\sim}{\tilde{\underline{B}}}$$

$$\tilde{\nabla} \times \underline{B} = i\underline{\kappa} \times \underset{\sim}{\tilde{\underline{B}}} .$$

$$\tilde{\nabla} p = i\underline{\kappa} \, \tilde{p}$$

$$\tilde{\nabla}^2 p = -\kappa^2 \tilde{p} ,$$

in which $\underline{\kappa} \equiv (\sin (k_x \Delta x)/\Delta x, \ k_y, \ k_z)$.

With the notation,

$$E \equiv \exp(-i\omega\Delta t) - 1$$
$$b \equiv (\underline{\kappa} \cdot \underline{v}_0) \Delta t$$
$$c \equiv (\underline{\kappa} \cdot \underline{B}_0) \Delta t$$
$$d \equiv \eta \kappa^2 \Delta t / 4S$$

$$f \equiv \nu \kappa^2 \Delta t,$$

substitution of these forms into (5) and (6) (linearized around $\underline{v} = \underline{v}_0 =$ const., $\underline{B} = \underline{B}_0 =$ const.) and use of the solenoidal conditions $\underline{\kappa} \cdot \underline{B} = \underline{\kappa} \cdot \underline{v} = 0$ leads to the simultaneous equations

$$\underline{B}^*(1 + 4d) = (1-ib)\underline{B}^n + ic\,\underline{v}^n$$

$$\underline{v}^* = (1-ib-f)\underline{v}^n + ic\,\underline{B}^n$$

$$\underline{B}^n E = ic\,\underline{v}^* - \underline{B}^*(ib+4d)$$

$$\underline{v}^n E = -(ib+f)\underline{v}^* + ic\,\underline{B}^*$$

and hence the dispersion relation

$$\left\{E + \frac{(ib+4d)(1-ib)}{1+4d} + c^2\right\}\left\{E + \frac{c^2}{1+4d} + (ib+f)(1-ib-f)\right\}$$

$$+ c^2\left\{1 - ib - f - \frac{(ib+4d)}{1+4d}\right\}\left\{\frac{1-ib}{1+4d} - (ib+f)\right\} = 0 .$$

(8)

It may be shown by a combination of analysis and numerical evaluation that this implies numerical stability for all values of d and gives the practical stability conditions $f \leqslant 1$, $|c| + |b| \leqslant 1$, the latter being the familiar Courant condition based on the combined Alfvén and flow speeds. The result is applied to the cylindrical case using the correspondance $\underline{\kappa} \to (1/\Delta r, m/r, k)$, in which m and k are the largest values present in the simulation.

Similarly, the dispersion relation for the case of implicit viscosity (implicit only on the first step) may be written

$$\left\{ E + \frac{(ib+4d)(1-ib)}{1+4d} + \frac{c^2}{1+f} \right\} \left\{ E + \frac{(ib+f)(1-ib)}{1+f} + \frac{c^2}{1+4d} \right\}$$

$$+ c^2 \left\{ \frac{1-ib}{1+4d} - \frac{ib+f}{1+f} \right\} \left\{ \frac{1-ib}{1+f} - \frac{ib+4d}{1+4d} \right\} = 0 \ .$$

Additionally, this implies numerical stability for all values of f.

Although the forward-time, centred-space scheme has already been ruled out on account of its intrinsic instability, it is nevertheless of interest to examine its MHD dispersion relation. This may be obtained directly from the first step of the 2-step scheme above. For the simplest case of a fully explicit scheme with no viscosity, the equations reduce to

$$(E + ib + 4d) \ \underline{B}^n \ = \ ic \ \underline{v}^n$$

$$(E + ib) \ \underline{v}^n \ = \ ic \ \underline{B}^n$$

and the dispersion relation becomes

$$\exp(-i\omega\Delta t) \ = \ 1 - 2d \pm \sqrt{(4d^2 - c^2)} - ib.$$

For $b = 0$, it follows that the region of numerical stability is bounded by the two curves

$$c^2 \leqslant 4d \qquad\qquad (0 \leqslant d \leqslant 1)$$

$$c^2 \geqslant 4(2d-1) \qquad\qquad (1/2 \leqslant d \leqslant 1)$$

and confirms the vanishing of numerical stability at large S ($d \to 0$). Despite claims to the contrary, this behaviour is also apparent in hybrid schemes [34] based on a forward-time advance to $\Delta t/2$ followed by a centred-time advance to Δt. For $b \neq 0$ (non-zero equilibrium flow), numerical stability further requires

$$c^2 > 2db^2$$

(approximately). This shows an unexpected second weakness of this method, namely destabilization by the plasma flow for all values of d.

The dispersion relation (8) also provides an expression for the numerical damping rate for Alfvén waves. For the case $b = 0$ (no equilibrium flow) and $f = 0$, its real and imaginary parts are

$$\exp(-\gamma\Delta t) \cos \omega_r \Delta t = 1 - \frac{c^2 + 2d(1+c^2)}{1 + 4d}$$

$$\exp(-\gamma\Delta t) \sin \omega_r \Delta t = \frac{\{c^2 - 4d^2(1 + c^2)^2\}^{1/2}}{1 + 4d}$$

(with notation $\omega \equiv \omega_r - i\gamma$). Using $d \ll 1$, $c < 1$ it follows that

$$\gamma \simeq \frac{\eta\kappa^2}{2S} + \frac{1}{2}(\underline{\kappa}\cdot\underline{B}_0)^2 \Delta t \quad .$$

The first term in this expression is the true physical damping rate. The second term is the additional numerical damping rate and is proportional to the timestep.

To understand the effect of time discretization more generally it is useful to complement the detailed calculation with the following discussion.

Suppose that a physical quantity Q varies as $\exp(-i\omega t)$, with physical frequency $\omega \equiv \omega_r - i\gamma$. The analytic time derivative is given by

$$\frac{\partial Q}{\partial t} = - i\omega \exp(-i\omega t)$$

whereas the numerical approximation to it is

$$\frac{\delta Q}{\delta t} = \frac{\exp\left[-i\omega(t+\Delta t)\right] - \exp(-i\omega t)}{\Delta t}$$

$$\simeq - \exp(-i\omega t)\ (i\omega + \frac{1}{2}\ \omega^2 \Delta t)$$

(assuming $|\omega|\Delta t \ll 1$). It is natural to describe the results of such time discretization in terms of a frequency ω_{num}, the numerical approximation to the true frequency ω, defined by

$$\frac{\delta Q}{\delta t} \equiv - i\omega_{num} \exp(-i\omega t).$$

It follows that

$$i\omega_{num} \simeq i\omega + \frac{1}{2}\,\omega^2 \Delta t$$

and hence that

$$(\omega_r)_{num} \simeq \omega_r - \omega_r \gamma \Delta t \tag{9}$$

$$\gamma_{num} \simeq \gamma + \frac{1}{2}\,(\omega_r^2 - \gamma^2)\,\Delta t.$$

These results are quite general, and do not depend on the nature of the spatial discretization.

For the Alfvén wave at high S, $\omega = \underline{k}\cdot\underline{B} = O(1)$, $\gamma = O(1/S)$ so that

$$(\omega_r)_{num} \simeq \omega_r$$

$$\gamma_{num} \simeq \gamma + \frac{1}{2}\,(\underline{k}\cdot\underline{B})^2 \Delta t$$

in agreement with the previous result.

3.4   Fourier representation and spatial derivatives in θ and z

An equally spaced mesh is used in θ and z. Derivatives in these directions are calculated by performing an FFT from physical space to Fourier space, multiplying by im (or ik) and transforming back to physical space.

The transforms are done using a highly efficient self-sorting, multiple-radix, multiple FFT routine for real data due to Temperton [35].

If there are N distinct mesh points in the direction under consideration (say θ), the physical grid point values are stored in N + 2 locations, the extra 2 locations containing copies of the periodic end values. This is shown in fig. 2a.

It is convenient to write the finite Fourier transform of these data in the form

$$f(\theta_i) = \sum_{m = -\left[\frac{N-1}{2}\right]}^{\left[N/2\right]} C_m \exp(im\theta_i) \qquad (10)$$

in which $C_m \equiv A_m + iB_m$ are the complex Fourier coefficients. Here the sum has been written over the fundamental Brillouin zone. With the convention that $\left[N/2\right]$ means division with truncation towards zero, this expression is correct for both N odd and N even.

Upon transformation, the Fourier coefficients

$$A_m + iB_m \equiv C_m = \frac{1}{N} \sum_{i=0}^{N-1} f(\theta_i) \exp(-im\theta_i)$$

overwrite the original data and are ordered as shown in fig. 2b. Values for negative m are not provided explicitly but may be obtained from the hermitean relation $C_{-m} = C_m^*$ that follows from the assumption of real data.

The reason for writing the Fourier transform in the principal zone as (10) rather than $0 \leqslant m \leqslant N - 1$ is that this form is necessary to obtain the correct value for the derivative by the process of multiplying by im.

For calculations that take place in transform space, notably the implicit treatment of resistivity and the calculation of energy spectra, it is necessary to follow the layout of the 4 numerical Fourier coefficients that arise for each m,n when transforms in θ and z are simultaneously in effect. The following diagrammatic approach has proved useful.

Let $f(\theta_i, z_j)$ be a doubly periodic real function. The Fourier transform in θ may be written

$$f(\theta_i, z_j) = \sum_m \{A_m(z_j) + iB_m(z_j)\} \exp im\theta_i$$

or in diagram form

$$\begin{bmatrix} A & B \end{bmatrix}_m$$

which also shows the ordering of the coefficients in computer memory. The assumption of real f gives the relations

$$A_{-m} = A_m \qquad B_{-m} = - B_m.$$

The transform in z is then written

$$A_m(z_j) = \sum_n (a_{mn} + ib_{mn}) \exp (ik_n z_j)$$

$$B_m(z_j) = \sum_n (c_{mn} + id_{mn}) \exp(ik_n z_j)$$

so that

$$f(\theta_i, z_j) = \sum_m \sum_n \left[(a_{mn} - d_{mn}) + i(b_{mn} + c_{mn})\right] \exp i(m\theta_i + k_n z_j) \; . \quad (11)$$

This may be represented as

$$\left[\begin{array}{cc} b & d \\ a & c \end{array}\right]_{m,n,}$$

with sign rules

a_{mn} does not change sign

b_{mn} changes sign with n   (12)

c_{mn} changes sign with m

d_{mn} changes sign with m and n .

As an example, if $f \equiv \cos(m\theta \pm k_n z)$, the transform in θ gives

$$f = \exp im\theta \left\{\tfrac{1}{2} \exp(\pm ik_n z)\right\} + \text{c.c.}$$

$$= \exp im\theta \left\{\tfrac{1}{2} \cos k_n z \pm \tfrac{i}{2} \sin k_n z\right\} + \text{c.c.}$$

so that

$$\left[\begin{array}{cc} A & B \end{array}\right] = \left[\tfrac{1}{2} \cos k_n z \quad \pm \tfrac{1}{2} \sin k_n z\right].$$

The transform in z then gives

$$A = \exp ik_n z \; (\tfrac{1}{4}) + c.c.$$

$$B = \exp ik_n z \; (\mp\tfrac{1}{4}) + c.c.$$

so that

$$\begin{bmatrix} b & d \\ a & c \end{bmatrix} = \begin{bmatrix} 0 & \mp 1/4 \\ 1/4 & 0 \end{bmatrix}.$$

The corresponding results for the transform of derivatives are obtained from

$$\frac{\partial f}{\partial \theta} = \sum_m im \, (A_m + iB_m) \exp im\theta$$

$$= \sum_m m \, (- B_m + iA_m) \exp im\theta$$

which may be represented as

$$m \begin{bmatrix} -B & A \end{bmatrix}_m.$$

The Fourier transform in z then gives

$$m \begin{bmatrix} -d & b \\ -c & a \end{bmatrix}_{m,n}.$$

i.e. a signed interchange in the θ direction.

The derivative in z is obtained from

$$\frac{\partial f}{\partial z} = \sum_m \left(\frac{\partial A_m}{\partial z} + i \frac{\partial B_m}{\partial z}\right) \exp im\theta$$

which may be represented as

$$\left[\begin{array}{cc} \frac{\partial A}{\partial z} & \frac{\partial B}{\partial z} \end{array}\right]_m.$$

The Fourier transform in z then gives

$$k \left[\begin{array}{cc} a & c \\ -b & -d \end{array}\right]_{m,n}$$

i.e. a signed interchange in the z direction.

The diagrams for second derivatives are obtained similarly:

$$\frac{\partial^2 f}{\partial \theta^2} = -m^2 \left[\begin{array}{cc} b & d \\ a & c \end{array}\right]_{m,n}$$

$$\frac{\partial^2 f}{\partial z^2} = -k^2 \left[\begin{array}{cc} b & d \\ a & c \end{array}\right]_{m,n}$$

$$\frac{\partial^2 f}{\partial z \partial \theta} = -mk \left[\begin{array}{cc} c & -a \\ -d & b \end{array}\right]_{m,n}.$$

3.5   Radial mesh and differencing in r

An equally spaced staggered mesh is used in the radial direction. The use of a staggered mesh is a basic feature of the MAC method and arises from the essential requirement that the numerical approximations to $\nabla\cdot$, ∇ and ∇^2 satisfy identically $\nabla^2 = \nabla\cdot\nabla$. This ensures that the pressure is calculated consistently in eqns. (5), (6), (7).

If all quantities were defined on an unstaggered mesh and $\nabla\cdot$, ∇ used standard central differences over $2\Delta r$, $\nabla^2 p$ would be defined over $4\Delta r$ (e.g. $p_{i+2} - 2p_i + p_{i-2}$) and would lead to decoupling of odd and even mesh points. This is usually an invitation to non-linear numerical "splitting" instability (formation of separate solutions on odd and even meshes) and is therefore to be avoided. In contrast, a staggered mesh overcomes this problem since ∇^2 can be derived consistently whilst still operating on neighbouring mesh values of p.

The layout of variables on the radial mesh is shown in fig. 3. The main feature is that B_r and v_r are carried at odd mesh points whereas B_θ, B_z and v_θ, v_z are carried at even mesh points.

In terms of the Fourier coefficients and with notation $i' = i + 1/2$, the fundamental numerical operators for point i on this mesh may be written

$$(\widetilde{\nabla}\cdot\underline{B})_i = \frac{(r\widetilde{B}_r)_{i'} - (r\widetilde{B}_r)_{i'-1}}{r_i \Delta r} + \frac{im}{r_i}(\widetilde{B}_\theta)_i + ik_n(\widetilde{B}_z)_i \qquad (13)$$

$$\left[(\tilde{\nabla} \times \underline{B})_r\right]_i = \frac{im}{r_i}(\tilde{B}_z)_i - ik_n(\tilde{B}_\theta)_i$$

$$\left[(\tilde{\nabla} \times \underline{B})_\theta\right]_{i\prime} = ik_n(\tilde{B}_r)_{i\prime} - \frac{(\tilde{B}_z)_{i+1} - (\tilde{B}_z)_i}{\Delta r} \tag{14}$$

$$\left[(\tilde{\nabla} \times B)_z\right]_{i\prime} = \frac{(r\tilde{B}_\theta)_{i+1} - (r\tilde{B}_\theta)_i}{r_{i\prime}\Delta r} - \frac{im}{r_{i\prime}}(\tilde{B}_r)_{i\prime}$$

$$(\tilde{\nabla}^2 p)_i = \frac{1}{\Delta r^2}\left[\tilde{p}_{i+1}\left(\frac{r_{i\prime}}{r_i}\right) - \tilde{p}_i\left(2 + \frac{m^2\Delta r^2}{r_i^2} + k_n^2\Delta r^2\right) + \tilde{p}_{i-1}\left(\frac{r_{i\prime-1}}{r_i}\right)\right]$$

The further quantities needed to evaluate the right hand sides of (5) and (6) are obtained from

$$\left[(\underline{v} \times \underline{B})_r\right]_i = (v_\theta)_i(B_z)_i - (v_z)_i(B_\theta)_i$$

$$\left[(\underline{v} \times \underline{B})_\theta\right]_{i\prime} = \frac{1}{2}\left[(v_z)_{i+1} + (v_z)_i\right](B_r)_{i\prime} -$$

$$\frac{1}{2}\left[(B_z)_{i+1} + (B_z)_i\right](v_r)_{i\prime}$$

$$\left[(\underline{v} \times \underline{B})_z\right]_{i\prime} = \frac{1}{2}\left[(B_\theta)_{i+1} + (B_\theta)_i\right](v_r)_{i\prime} -$$

$$\frac{1}{2}\left[(v_\theta)_{i+1} + (v_\theta)_i\right](B_r)_{i\prime}$$

- 28 -

$$(\partial \tilde{p}/\partial r)_{i'} = \frac{\tilde{p}_{i+1} - \tilde{p}_i}{\Delta r}$$

$$(\partial \tilde{p}/r \partial \theta)_i = (im/r_i)\, \tilde{p}_i$$

$$(\partial \tilde{p}/\partial z)_i = ik_n \tilde{p}_i$$

$$\left[(-\underline{v} \cdot \nabla \underline{v})_r\right]_{i'} = \frac{1}{r_{i'} \Delta r} \left\{ \frac{1}{4} \left[(rv_r)_{i'} + (rv_r)_{i'-1}\right]\left[(v_r)_{i'} + (v_r)_{i'-1}\right]\right.$$

$$\left. - \frac{1}{4} \left[(rv_r)_{i'+1} + (rv_r)_{i'}\right]\left[(v_r)_{i'+1} + (v_r)_{i'}\right] \right\}$$

$$- \frac{1}{r_{i'}} \frac{\delta}{\delta\theta} \left\{ \frac{1}{2} \left[(v_\theta)_{i+1} + (v_\theta)_i\right] (v_r)_{i'}\right\}$$

$$- \frac{\delta}{\delta z} \left\{ \frac{1}{2} \left[(v_z)_{i+1} + (v_z)_i\right] (v_r)_{i'}\right\}$$

$$+ \frac{1}{4r_{i'}} \left[(v_\theta)_{i+1} + (v_\theta)_i\right]^2$$

$$\left[(-\underline{v}\cdot\nabla\underline{v})_\theta\right]_i = \frac{(rv_r)_{i'-1}\,\frac{1}{2}\left[(v_\theta)_i + (v_\theta)_{i-1}\right] - (rv_r)_{i'}\,\frac{1}{2}\left[(v_\theta)_{i+1} + (v_\theta)_i\right]}{r_i\,\Delta r}$$

$$- \frac{1}{r_i}\frac{\delta}{\delta\theta}(v_\theta)_i^2 - \frac{\delta}{\delta z}\left[(v_z)_i\,(v_\theta)_i\right]$$

$$- \frac{1}{2r_i^2}\left[(rv_r)_{i'} + (rv_r)_{i'-1}\right](v_\theta)_i$$

$$\left[(-\underline{v}\cdot\nabla\underline{v})_z\right]_i = \frac{(rv_r)_{i'-1}\,\frac{1}{2}\left[(v_z)_i + (v_z)_{i-1}\right] - (rv_r)_{i'}\,\frac{1}{2}\left[(v_z)_{i+1} + (v_z)_i\right]}{r_i\,\Delta r}$$

$$- \frac{1}{r_i}\frac{\delta}{\delta\theta}\left[(v_\theta)_i\,(v_z)_i\right] - \frac{\delta}{\delta z}(v_z)_i^2$$

$$\left[(\underline{j}\times\underline{B})_r\right]_{i'} = (j_\theta)_{i'}\,\frac{1}{2}\left[(B_z)_{i+1} + (B_z)_i\right] - (j_z)_{i'}\,\frac{1}{2}\left[(B_\theta)_{i+1} + (B_\theta)_i\right]$$

$$\left[(\underline{j}\times\underline{B})_\theta\right]_i = \frac{1}{4}\left[(j_z)_{i'} + (j_z)_{i'-1}\right]\left[(B_r)_{i'} + (B_r)_{i'-1}\right] - (j_r)_i\,(B_z)_i$$

$$\left[(\underline{j}\times\underline{B})_z\right]_i = (j_r)_i(B_\theta)_i - \frac{1}{4}\left[(j_\theta)_{i'} + (j_\theta)_{i'-1}\right]\left[(B_r)_{i'} + (B_r)_{i'-1}\right].$$

It can be seen that an averaging procedure has to be employed in certain places to obtain values on the appropriate mesh. The viscosity term $\nu\nabla^2\underline{v}$ is calculated as $-\nu\nabla \times \underline{\omega}$, $\underline{\omega} = \nabla \times \underline{v}$. The importance of the numerical form of $\underline{v} \cdot \nabla\underline{v}$ has been stressed elsewhere [36].

An alternative approach to the calculation of $\underline{v} \cdot \nabla\underline{v}$, and one which may have some advantages is to evaluate it as $\nabla(v^2/2) + \underline{\omega} \times \underline{v}$.

3.6   Regularity conditions at the origin

A feature of a polar mesh is the singular point at the origin. This prohibits the application of the finite difference expressions and forces a special treatment, based on the analytic properties of the physical variables involved.

The first step is to identify the analytic conditions that must be satisfied at the origin. This may be accomplished by the following (widely used) arguments, based on considerations of regularity and single-valuedness. For a scalar field such as pressure, with Fourier representation

$$p(r,\theta,z) = \sum_m \tilde{p}(r,z) \exp im\theta,$$

the derivative $\partial p/\partial x$ exists and is given by

$$\frac{\partial p}{\partial x} = \frac{\partial p}{\partial r} \cos\theta - \frac{\partial p}{\partial \theta} \frac{\sin\theta}{r}$$

$$= \frac{1}{2} \sum_m \exp i(m+1)\theta \left\{\frac{\partial \tilde{p}_m}{\partial r} - \frac{m\tilde{p}_m}{r}\right\} + \exp i(m-1)\theta \left\{\frac{\partial \tilde{p}_m}{\partial r} + \frac{m\tilde{p}_m}{r}\right\}.$$

Single-valuedness at the origin then requires

$$\lim_{r \to 0} \left(\frac{\partial \tilde{p}_m}{\partial r} - \frac{|m|\tilde{p}_m}{r}\right) = 0 \qquad |m| = 1$$

$$\lim_{r \to 0} \frac{\partial \tilde{p}_m}{\partial r} = \lim_{r \to 0} \frac{m\tilde{p}_m}{r} = 0 \qquad |m| \neq 1$$

and hence

$$\frac{\partial \tilde{p}_m}{\partial r} \to 0 \qquad m = 0 \tag{15}$$

$$\tilde{p}_m \to 0 \qquad m \neq 0. \tag{16}$$

For a vector field such as $\underline{B}$, the cartesian component B_z has properties identical to those of p. The components B_r and B_θ are investigated by writing

$$B_x = B_r \cos\theta - B_\theta \sin\theta$$

$$= \frac{1}{2} \sum_m \exp i(m+1)\theta \left\{\tilde{B}_{rm} + i\tilde{B}_{\theta m}\right\} + \exp i(m-1)\theta \left\{\tilde{B}_{rm} - i\tilde{B}_{\theta m}\right\}.$$

Single-valuedness of B_x then requires

$$\tilde{B}_{rm} + im\,\tilde{B}_{\theta m} \to 0 \qquad\qquad |m| = 1$$

$$\tilde{B}_{rm} \to 0 \qquad\qquad |m| \neq 1 \qquad\qquad\qquad (17)$$

$$\tilde{B}_{\theta m} \to 0 \qquad\qquad |m| \neq 1.$$

The second step is to implement these conditions numerically. For $m > 1$ this is trivial since all quantities vanish at the origin. Some discussion is needed however for $m = 0$ and $m = 1$.

For $m = 1$, condition (17) has been implemented by setting $\tilde{B}_\theta$ at the origin equal to $\tilde{B}_r$ at the point $r = \Delta r/2$ (with the necessary change of phase). This procedure is accurate to $O(\Delta r^2)$ and has caused no problems in practice.

For $m = 0$, the derivative condition (15) on p and B_z has been implemented by setting $\tilde{p}(1) = \tilde{p}(2)$ and $\tilde{B}_z(1) = \tilde{B}_z(2)$, a conventional treatment. However this has the result that $\partial\tilde{p}/\partial r$ and $\tilde{j}_\theta$ are numerically zero for $m = 0$ at the point $r = \Delta r/2$ and hence that the forces around this point cannot be evaluated accurately for $m = 0$.

Probably as a result of this intrinsic inaccuracy, some numerical difficulties have been experienced with $m = 0$ modes, particularly the onset of a linear numerical instability with $\tilde{v}_r$ becoming singular near the origin.

The current resolution of this problem has been to set the radial force $\tilde{Q}_r$ ($\underline{Q} \equiv -\underline{v} \cdot \nabla \underline{v} + \underline{j} \times \underline{B} + \nu \nabla^2 \underline{v}$) to zero for $m = 0$ at the point $r = \Delta r/2$. With the condition $\partial \tilde{p}/\partial r = 0$ there, this means that the $m = 0$ component of $\tilde{v}_r$ is fixed (usually zero) for all time at that point. Since $\tilde{Q}_r \sim r$, $\tilde{v}_r \sim r$ for $m = 0$ in the neighbourhood of the origin, the accuracy of this procedure is consistent with the typical truncation error there. The $m = 0$ modes are generally well-behaved (but not perfect) when this procedure is adopted. A tidy consequence of $\tilde{v}_r = 0$ and $\tilde{j}_\theta = 0$ for $m = 0$ at point $r = \Delta r/2$ is that the $m = 0$ component of $\tilde{B}_r$ there is also fixed (usually zero) for all time.

Although the above procedure has provided a tactical solution, a full resolution of the difficulty requires an improved strategy. At the expense of some complication it is proposed to keep the current mesh but calculate the central value of p by quadratic interpolation. An alternative approach which may offer some advantage is to change the layout of variables at the origin such that $\partial p/\partial r$ rather than p is to be calculated there.

3.7 Boundary conditions

The following conventional, highly idealized boundary conditions are used. The plasma is assumed to be bounded by a perfectly conducting impermeable wall so that

$$B_r = v_r = 0$$

at $r = 1$.

The system is driven by imposing a uniform electric field at the wall through

$$E_\theta = (\eta/S)j_\theta \tag{18}$$

$$E_z = (\eta/S)j_z$$

in which E_θ and E_z are given.

The r component of the momentum equation at the wall gives the (Neumann) boundary condition on the pressure

$$\frac{\partial p}{\partial r} = \frac{v_\theta^2}{r} + j_\theta B_z - j_z B_\theta + \nu(\nabla^2 \underline{v})_r \equiv Q_r. \tag{19}$$

For the inviscid case, the conditions above are sufficient to give a well defined problem and therefore no physical boundary conditions must be specified for B_θ, B_z, v_θ, v_z. Furthermore, owing to the use of a staggered mesh, not even numerical values of these quantities are needed at the boundary.

The magnetic flux Φ in the cylinder is fixed by the initial conditions.

For the viscid case, extra boundary conditions are required and are applied here by specifying values of ω_θ and ω_z at the walls consistent

with free-slip (an arbitrary choice, but one least likely to cause unwanted viscous boundary phenomena). This choice leads to the requirement

$$\omega_\theta = 0$$

$$\omega_z = 2 v_\theta / r.$$

It should be noted that the boundary condition $\underline{n} \times \underline{\omega} = 0$ sometimes used in MHD calculations represents free-slip only in cartesian geometry. Physically, the correctness of the above conditions may be seen by considering a simple example of free-slip motion, namely that comprising a rigid body rotation with angular frequency Ω and a uniform translation with velocity v_z. It follows that

$$\omega_\theta = - \frac{\partial v_z}{\partial r} = 0$$

$$\omega_z = \frac{1}{r} \frac{\partial}{\partial r} (r^2 \Omega) = 2\Omega = \frac{2v_\theta}{r},$$

in agreement with the above result.

3.8   Solution of the pressure equation

At each timestep, the pressure is calculated from the Poisson equation (7) which in numerical form leads to the tridiagonal system

$$a_i \tilde{p}_{i-1} + b_i \tilde{p}_i + c_i \tilde{p}_{i+1} = \tilde{d}_i \Delta r^2 \tag{20}$$

$(2 \leq i \leq N_r - 1)$. Here,

$$a_i \equiv r_{i-1}/r_i$$

$$b_i \equiv - \left[2 + (m^2/r_i^2 + k_n^2) \Delta r^2 \right]$$

$$c_i \equiv r_i \diagup r_i$$

and d is the source term given by

$$d \equiv \frac{1}{\Delta t} \nabla \cdot \underline{v}^n + \nabla \cdot \underline{Q}^n \qquad (21)$$

in which

$$\underline{Q}^n \equiv - \underline{v}^n \cdot \nabla \underline{v}^n + \underline{j}^n \times \underline{B}^n + \nu \nabla^2 \underline{v}^n.$$

As discussed above, the conditions at the origin are simply $\tilde{p}_1 = 0$ for
$m \neq 0$ (16) and $\tilde{p}_1 = \tilde{p}_2$ for $m = 0$ (15). These are implemented through the
equations

$$\tilde{p}_1 + 0 \cdot \tilde{p}_2 = 0 \quad (m \neq 0)$$

$$\qquad (22)$$

$$\tilde{p}_1 - 1 \cdot \tilde{p}_2 = 0 \quad (m = 0).$$

The case $m = 0$, $k = 0$ is special since it is not possible to specify a
derivative condition simultaneously at the origin and the boundary.
Instead, $\tilde{p}$ must be given a specific value at the wall. This is

consistent with the fact that the pressure in an incompressible fluid is known only to within an additive constant. The pressure gradient at the wall then automatically takes up its correct value.

The Neumann boundary conditions (19) are constructed by introducing a fictitious point at r_{N+1} and using centred differences to write

$$\tilde{p}_{N+1} - \tilde{p}_N = (\tilde{Q}_r)_N \cdot \Delta r .$$

Elimination of $\tilde{p}_{N+1}$ in (20) gives the final equation

$$a_N \tilde{p}_{N-1} + (b_N + c_N) \tilde{p}_N = \tilde{d}_N \Delta r^2 - c_N (\tilde{Q}_r)_N \cdot \Delta r . \tag{23}$$

An interesting cancellation occurs for Q_r in the right hand side of (23). On writing out the source term d from (21), the terms in Q_r in (23) are simply

$$+ \frac{\left[(r\tilde{Q}_r)_{N'} - (r\tilde{Q}_r)_{N'-1} \right] \Delta r}{r_N} - \frac{r_{N'}}{r_N} (\tilde{Q}_r)_{N'} \cdot \Delta r,$$

showing that the term in $(Q_r)_{N'}$ vanishes identically. This is a valuable practical feature since this quantity is not actually calculable on the present mesh. This property of the boundary conditions has been noted elsewhere [37].

3.9   Implicit treatment of resistivity

The first step of the time advancement scheme requires the solution of the implicit system

$$\underline{B}^* + \Delta t \, (\nabla \times \gamma \, \nabla \times \underline{B}^*) = \underline{D}. \tag{24}$$

Here $\underline{B}^*$ is to be found, $\gamma \equiv \eta/S$ (for notational convenience below) and the source term D is given by

$$\underline{D} \equiv \underline{B}^n + \Delta t \, \nabla \times (\underline{v}^n \times \underline{B}^n).$$

Using the expressions (14) for the components of curl (and the equivalent expressions for the alternative mesh points), the following linear block tridiagonal equations are obtained for the complex Fourier coefficients $i\widetilde{B}_r$, $\widetilde{B}_\theta$, and $\widetilde{B}_z$:

$$\left[1 + \gamma_i \, \Delta t \left(\frac{m^2}{r_i^2} + k^2 \right) \right] (i\widetilde{B}_r)_i + \left[\frac{m r_i \, \gamma_i \, \Delta t}{r_i^2 \, \Delta r} \right] (\widetilde{B}_\theta)_i$$

$$+ \left[\frac{-m r_{i+1} \, \gamma_i \, \Delta t}{r_i^2 \, \Delta r} \right] (\widetilde{B}_\theta)_{i+1} + \left[\frac{k \gamma_i \, \Delta t}{\Delta r} \right] (\widetilde{B}_z)_i$$

$$+ \left[\frac{-k \gamma_i \, \Delta t}{\Delta r} \right] (\widetilde{B}_z)_{i+1} = (i\widetilde{D}_r)_i.$$

$$\left[\frac{m\gamma_{i'}\Delta t}{r_{i'}\Delta r}\right](i\tilde{B}_r)_{i'} \; + \; \left[\frac{-m\gamma_{i'-1}\Delta t}{r_{i'-1}\Delta r}\right](i\tilde{B}_r)_{i'-1}$$

$$+ \; \left[1 + \Delta t\left(k^2\gamma_i \; + \; \frac{r_i\gamma_{i'-1}}{r_{i'-1}\Delta r^2} \; + \; \frac{r_i\gamma_{i'}}{r_{i'}\Delta r^2}\right)\right](\tilde{B}_\theta)_i \; +$$

$$\left[\frac{-r_{i+1}\gamma_{i'}\Delta t}{r_i\Delta r^2}\right](\tilde{B}_\theta)_{i+1} \; + \; \left[\frac{-r_{i-1}\gamma_{i'-1}\Delta t}{r_{i'-1}\Delta r^2}\right](\tilde{B}_\theta)_{i-1} \; +$$

$$\left[\frac{-mk\gamma_i\Delta t}{r_i}\right](\tilde{B}_z)_i \; = \; (\tilde{D}_\theta)_i$$

$$\left[\frac{r_{i'}\gamma_{i'}k\Delta t}{r_i\Delta r}\right](i\tilde{B}_r)_{i'} + \left[\frac{-r_{i'-1}\gamma_{i'-1}k\Delta t}{r_i\Delta r}\right](i\tilde{B}_r)_{i'-1}$$

$$+ \; \left[\frac{-m\gamma_i k\Delta t}{r_i}\right](\tilde{B}_\theta)_i \; + \; \left[1 + \Delta t\left(\frac{m^2\gamma_i}{r^2_i} + \frac{r_{i'}\gamma_{i'}}{r_i\Delta r^2} + \frac{r_{i'-1}\gamma_{i'-1}}{r_i\Delta r^2}\right)\right](\tilde{B}_z)_i$$

$$+ \; \left[\frac{-r_{i'}\gamma_{i'}\Delta t}{r_i\Delta r^2}\right](\tilde{B}_z)_{i+1} + \left[\frac{-r_{i'-1}\gamma_{i'-1}\Delta t}{r_i\Delta r^2}\right](\tilde{B}_z)_{i-1} = (\tilde{D}_z)_i$$

In accordance with the rules described in section 3.4, the complex Fourier coefficients appearing in these equations must be interpreted as the diagrams

$$(i\widetilde{B}_r) \equiv \begin{bmatrix} -d & b \\ -c & a \end{bmatrix}$$

$$(\widetilde{B}_\theta) \equiv \begin{bmatrix} b & d \\ a & c \end{bmatrix} \tag{25}$$

$$(\widetilde{B}_z) \equiv \begin{bmatrix} c & -a \\ -d & b \end{bmatrix}$$

and similarly for the source term $\underline{D}$.

At the wall, the boundary condition $B_r = 0$ is implemented by the trivial equation

$$1 \cdot (i\widetilde{B}_r)_{N'} = 0.$$

Application of the electric field boundary condition (18) leads to modified θ and z equations for the point $i = N$:

$$\left[\frac{-m\gamma_{N'-1}\,\Delta t}{r_{N'-1}\,\Delta r}\right](i\widetilde{B}_r)_{N'-1} + \left[1 + \Delta t\left(k^2\gamma_N + \frac{r_N\gamma_{N'-1}}{r_{N'-1}\,\Delta r^2}\right)\right](\widetilde{B}_\theta)_N +$$

$$\left[\frac{-r_{N-1}\gamma_{N'-1}\,\Delta t}{r_{N'-1}\,\Delta r^2}\right](\widetilde{B}_\theta)_{N-1} + \left[\frac{-mk\gamma_N\,\Delta t}{r_N}\right](\widetilde{B}_z)_N = (\widetilde{D}_\theta)_N + \frac{\widetilde{E}_z\,\Delta t}{\Delta r}$$

$$\left[\frac{-r_{N'-1}\gamma_{N'-1}k\Delta t}{r_N\Delta r}\right](i\widetilde{B}_r)_{N'-1} \quad + \quad \left[\frac{-mk\gamma_N\Delta t}{r_N}\right](\widetilde{B}_\theta)_N$$

$$+ \quad \left[1 + \Delta t\left(\frac{m^2\gamma_N}{r_N^2} + \frac{r_{N'-1}\gamma_{N'-1}}{r_N\Delta r^2}\right)\right](\widetilde{B}_z)_N \quad + \quad \left[\frac{-r_{N'-1}\gamma_{N'-1}\Delta t}{r_N\Delta r^2}\right](\widetilde{B}_z)_{N-1}$$

$$= \quad (\widetilde{D}_z)_N \quad - \quad \frac{r_{N'}\widetilde{E}_\theta\Delta t}{r_N\Delta r} \, .$$

Since the imposed electric fields are uniform, the contributions from E_θ and E_z apply only to $m = 0$, $k = 0$.

At the origin, the regularity conditions of section 3.6 are implemented by means of the equations

$$(\widetilde{B}_\theta)_1 \qquad\qquad\qquad\qquad = \ 0 \qquad m \neq 1$$

$$(\widetilde{B}_\theta)_1 \quad - \quad (i\widetilde{B}_r)_{1'} \qquad = \ 0 \qquad m = 1 \qquad\qquad (26)$$

$$(\widetilde{B}_z)_1 \qquad\qquad\qquad\qquad = \ 0 \qquad m \neq 0$$

$$(\widetilde{B}_z)_1 \quad - \quad (\widetilde{B}_z)_2 \qquad\quad = \ 0 \qquad m = 0,$$

correct to $O\left(\Delta r^2\right)$.

The formulation of the linear system is completed by the calculation of the source term $\underline{D}$. Using the notation

$$\underline{T} \equiv \underline{v} \times \underline{B},$$

and the diagram rules of section 3.4, it may be written

$$(i\tilde{D}_r)_{i\prime} = (i\tilde{B}_r)_{i\prime} - \frac{m\Delta t}{r_{i\prime}} (\tilde{T}_z)_{i\prime} + k\Delta t\, (\tilde{T}_\theta)_{i\prime}$$

$$(\tilde{D}_\theta)_i = (\tilde{B}_\theta)_i + k\Delta t\, (i\tilde{T}_r)_i - \frac{\Delta t}{\Delta r}\left[(\tilde{T}_z)_{i\prime} - (\tilde{T}_z)_{i\prime-1}\right]$$

$$(\tilde{D}_z)_i = (\tilde{B}_z)_i + \frac{\Delta t}{r_i \Delta r}\left[(r\tilde{T}_\theta)_{i\prime} - (r\tilde{T}_\theta)_{i\prime-1}\right] - \frac{m\Delta t}{r_i} (i\tilde{T}_r)_i$$

in which $\underline{B}$ and $\underline{D}$ represent the diagrams shown in (25) and $\underline{T}$ represents the diagrams

$$i\tilde{T}_r \equiv \begin{bmatrix} a & c \\ -b & -d \end{bmatrix}$$

$$\tilde{T}_\theta \equiv \begin{bmatrix} c & -a \\ -d & b \end{bmatrix}$$

$$\tilde{T}_z \equiv \begin{bmatrix} b & d \\ a & c \end{bmatrix}.$$

The block tridiagonal system is solved by the block version of the standard algorithm for tridiagonal systems.

For efficiency the explicit form of the matrix inverse of the blocks
has been used and explicit account taken of their sparsity pattern.

3.10   De-aliasing in θ and z

As described in the introduction to section 3, it is essential that
non-linear calculations are de-aliased to prevent the development of
numerical instability that would otherwise occur. This section gives more
detail to that discussion.

A simple view of the aliasing process relevant here can be obtained by
considering, for instance, the representation of the function $v = \cos 4\theta$
on a mesh with 8 points, and the calculation of the typical non-linear
term v^2.

In a continuous system the result would be $v^2 = (1 + \cos 8\theta)/2$, reducing
to $v^2 = 1/2$ if high mode numbers were discarded.

In contrast, on the mesh, the values of $\cos 4\theta$ are simply ± 1, so that
$v^2 = 1$. This discrepancy arises because although $\cos 8\theta$ has sub
grid-scale variation, it appears on the mesh as a constant.   This
erroneous appearance of energy at low mode number from unresolvably high
mode numbers constitutes the aliasing error.

Furthermore, it is apparent that this effect opens the possibility of a
non-physical positive feedback loop in k-space and consequent numerical
instability. A detailed analysis [38] predicts the existence of an
'explosive' non-linear instability of the form B, $v \sim 1/(t_c - t)$, in which

t_c is an undetermined critical constant. This is in good agreement with the results from a non-linear test case, presented in section 6.1.

A straightforward resolution of this problem in θ and z is provided by discarding the upper part of the Fourier spectrum of all field quantities. In general, the aliasing interaction of mode numbers m_1 and m_2 to produce a lower mode number m is described by the expression

$$m = (m_1 + m_2) \bmod N$$

in which N is the number of mesh points. If m* is the largest m value that is not a source of aliasing error, it satisfies

$$2m^* - N < -m^*$$

so that

$$m^* < N/3. \tag{27}$$

This shows that the calculation can be de-aliased in θ (and similarly z) by setting to zero all Fourier coefficients with $m \geqslant N/3$. It corresponds to using only 2/3 of the available Fourier modes for each dimension and is equivalent to a Galerkin approximation.

3.11   Radial aliasing and additional velocity smoothing

In the inviscid case, the velocity field in the present code can develop non-physical radial spikes (even when de-aliased in θ and z) if the

calculation becomes sufficiently non-linear. Such a calculation may eventually fail with an explosive numerical instability, identifiable as non-physical by the gross non-conservation of energy.

This behaviour is attributed to aliasing error in the radial (finite difference) direction driving an unstable positive feedback loop in k_r space. Experience shows that the velocity is always less numerically robust than the magnetic field.

The presence of aliasing error is a fundamental weakness of elementary finite difference methods for low dissipation non-linear simulations. Unfortunately, the problem is harder to treat than in the spectral directions θ and z since the same easy access to the troublesome wavenumbers is not available.

The resolution adopted here, as in similar finite difference codes, is the addition of a small amount of viscosity (typical magnitude $\nu \leqslant 1/S$) in order to smooth the velocity spikes. This approach appears to be satisfactory for the simulations of immediate interest (the Reversed Field Pinch), but more generally raises the obvious question of the effect of this additional viscosity on the physical processes being simulated.

4. Diagnostic facilities

The code has been equipped with a considerable number of diagnostics. In addition to various 1D, 2D and 3D plots of current, magnetic field and velocity field, there are facilities to monitor the following quantities: $\nabla \cdot \underline{B}$ and $\nabla \cdot \underline{v}$; longitudinal flux, total z-momenta, total energy (conserved

quantities); energy spectra; mean fields at the wall, total current, $j_{\parallel}$
and $j_{\perp}$, $\underline{v} \times \underline{B}$, $\int \underline{A} \cdot \underline{B}$ (for RFP simulations); magnetic island growth rates
(for tearing mode simulations). These quantities are usually plotted
versus time ('history plots').

Many of these diagnostic quantities involve elementary numerical
evaluation, which will not be described further. Some topics of wider
interest are discussed below.

4.1   Radial integration method

Many of the above quantities involve integration in space. For the θ and
z directions the standard theory of numerical integration of periodic
functions indicates the use of the trapezoidal rule [39].

A 3-point integration rule is used in the radial direction. Excluding the
origin (for quantities defined on odd mesh points) or the boundary (for
quantities defined on even mesh points), the mesh is equally spaced and
the 3-point scheme is simply Simpson's rule

$$\int_0^{2\Delta r} f \ dr \ \simeq \ \frac{\Delta r}{3} \left\{ f(0) \ + \ 4f(\Delta r) \ + \ f(2\Delta r) \right\}.$$

However, where appropriate, integration to the boundary or origin involves
the mesh spacings (Δr, Δr, $\Delta r/2$). Calculation of the integration
coefficients in the standard way [40] gives the integration rule

$$\int_0^{5\Delta r/2} f \ dr \ \simeq \ \frac{\Delta r}{24} \left\{ 10f(0) \ + \ 25f(\Delta r) \ + \ 25f(2\Delta r) \right\}.$$

Multiple application of the 3-point rule covers the case of N_r odd. For N_r even, the extra point is absorbed by one application of the 4-point rule

$$\int_0^{3\Delta r} f \, dr \simeq \frac{3\Delta r}{8} \left\{ f(0) + 3f(\Delta r) + 3f(2\Delta r) + f(3\Delta r) \right\}.$$

Fig. 4 shows the final layout of the integration coefficients.

4.2 $\nabla \cdot B$ and $\nabla \cdot v$

The divergence is computed on even mesh points from (13) and is displayed by plotting the maximum absolute value. Fig. 5 shows typical results. $\nabla \cdot \underline{v}$ is maintained at an almost constant roundoff level by the MAC algorithm by virtue of the intrinsic correction of $\underline{v}$ at each timestep. In contrast, $\nabla \cdot \underline{B}$ drifts slowly upwards owing to the accumulation of rounding error (but is still extremely small).

4.3   Conservation properties

As a check on the global accuracy of a simulation run it is important to monitor the numerical conservation or otherwise of invariant quantities.

The simplest invariant quantity is the total longitudinal magnetic flux

$$\Phi \equiv \int B_z \, r \, dr \, d\theta$$

which from (3) satisfies the exact conservation relation

$$\Phi \; + \; 2\pi \int E_\theta \; dt \; = \; \text{const.}$$

and is therefore conserved when $E_\theta = 0$ (a common case).

Two further quantities monitored in the code are the total z angular momentum

$$L_z \; \equiv \; \int \rho r v_\theta \; d\tau$$

and the total z linear momentum

$$P_z \; \equiv \; \int \rho v_z \; d\tau.$$

These satisfy the equations

$$\frac{\partial L_z}{\partial t} \; + \; \int \rho r v_\theta \; \underline{v} \cdot \underline{dS} \; - \; \int r B_\theta \; \underline{B} \cdot \underline{dS} \; - \; \nu \int (r \omega_z - 2 v_\theta) \; dS = 0$$

$$\frac{\partial P_z}{\partial t} \; + \; \int \rho v_z \; \underline{v} \cdot \underline{dS} \; - \; \int B_z \; \underline{B} \cdot \underline{dS} \; + \; \int (p + B^2/2) \; \underline{z} \cdot \underline{dS} \; - \; \nu \int \omega_\theta dS = 0$$

and are thus conserved in the present system of a periodic cylinder with free slip and $v_r = B_r = 0$ at the walls.

The most important invariant quantity monitored by the code is the total energy. This satisfies the conservation law

$$\frac{\partial U}{\partial t} \; \equiv \; \frac{\partial}{\partial t} \int (B^2/2 + v^2/2) \; d\tau \; + \; E_\theta \int B_z \; dS \; - \; E_z \int B_\theta \; dS$$

$$+ (\eta/S) \int \underline{j}^2 \, d\tau - \nu \int \underline{v} \cdot \nabla^2 \underline{v} \, d\tau = 0.$$

Here U is the total energy and comprises the total magnetic energy, the total kinetic energy, the total Poynting flux at the wall, the total Joule heating and the total viscous dissipation.

The importance of the energy conservation law is that it gives an unambiguous check on the presence of numerical instability for then the energy is not conserved even approximately but grows without limit.

Even in a simulation that is numerically stable, the total energy will not be conserved exactly but will decay to some extent owing to the effect of non-physical numerical dissipation.

4.4   Calculation of energy spectra

One of the most useful diagnostics in the code is the calculation of the energy spectrum (the energy in each of the Fourier modes of any component of $\underline{B}$ or $\underline{v}$) since it provides a clear picture of the MHD activity in any simulation.

Although the calculation of the energy spectrum is simply an application of Parseval's theorem, its implementation is somewhat more complicated. In particular a convention has to be chosen for the region of mode number (m,n) space in which the results are to be presented.

The version of Parseval's theorem needed here may be demonstrated in 1D. Starting from the Fourier representation (10), it follows that

$$\sum_{i=0}^{N-1} \left| f(\theta_i) \right|^2 = \sum_{m=-\left[\frac{N-1}{2}\right]}^{\left[N/2\right]} \sum_{m'=-\left[\frac{N-1}{2}\right]}^{\left[N/2\right]} C_m C_{m'}^* \sum_{i=0}^{N-1} \exp i(m - m')\theta_i \,.$$

Using the relation

$$\sum_{i=0}^{N-1} \exp i(m - m')\theta_i = N \, \delta_{m, m' + \alpha N} \tag{28}$$

and noting that $\alpha = 0$ is the only accessible zone, this reduces to

$$\sum_{i=0}^{N-1} \left| f(\theta_i) \right|^2 = N \sum_{m=-\left[\frac{N-1}{2}\right]}^{\left[N/2\right]} C_m C_m^* \,.$$

For the application below, this result is needed in terms of a sum over non-negative m. Using $C_m^* = C_{-m}$ for real data, the expressions are

$$\frac{1}{N} \sum_{i=0}^{N-1} \left| f(\theta_i) \right|^2 = C_0^2 + 2 \sum_{m=1}^{\left[N/2\right]} C_m C_m^* \qquad \text{for N odd} \tag{29}$$

$$= C_0^2 + 2 \sum_{m=1}^{\left[N/2\right]-1} C_m C_m^* + C_{N/2} C_{N/2} \quad \text{for N even.}$$

The convention about the region of interest in (m,n) space may be illustrated as follows. Although the double Fourier transform

$$f = \sum_{m,n} C_{mn} \exp i(m\theta + k_n z)$$

formally involves 4 types of term (all combinations of

exp $i(\pm|m|\theta \pm |k_n|z))$, these may equally well be written as

exp $\pm i(|m|\theta \pm |k_n|z)$, showing that only 2 (those of opposite helicities) are physically distinct. For present purposes the following convention has therefore been adopted: m is taken to be non-negative but n has either sign; in the case m = 0 the helicities are degenerate and n is restricted to non-negative values.

The expression for the energy spectrum is then obtained by approximating the quadratic integral

$$I \equiv \int_0^L \int_0^{2\pi} \int_0^1 |f|^2 \, r \, dr \, d\theta \, dz$$

by trapezoidal sums in θ and z and using Parseval's theorem above to give the result

$$I \simeq \sum_{m=0}^{\left[N_\theta/2\right]} \sum_{n=-\left[\frac{N_z-1}{2}\right]}^{\left[N_z/2\right]} I_{mn} .$$

Here,

$$I_{mn} \equiv (2) \; 2\pi L \int_0^1 |C_{mn}|^2 \, r \, dr$$

is defined to be the energy spectrum value for helicity (m,n). The selective factor 2 enters according to (29). The sign rules (12) are used to calculate the Fourier coefficients for negative n. The results are usually displayed as $I_{mn}^{1/2}$.

4.5   Calculation of $\int \underline{A} \cdot \underline{B}$

The quantity

$$K \equiv \int \underline{A} \cdot \underline{B} \, d\tau$$

is of interest owing to its central position in the relaxation theory of field reversal [41]. The method of calculation is based on an idea by M.K. Bevir [42].

The two basic features of the approach are first that the gauge is chosen such that $A_r = 0$ and A_z has zero mean, and secondly that $\underline{A}$ is not computed explicitly, but is expressed in terms of $\underline{B}$.

The formal expression for K in the discrete system is obtained by expressing $\underline{A}$ and $\underline{B}$ in terms of their double Fourier transforms, using the trapezoidal rule to approximate the integrals in θ and z, and then using (28) to obtain the expression

$$K = 2\pi L \sum_{m=-\left[\frac{N_\theta - 1}{2}\right]}^{\left[N_\theta/2\right]} \sum_{n=-\left[\frac{N_z - 1}{2}\right]}^{\left[N_z/2\right]} K_{mn} \tag{30}$$

in which

$$K_{mn} \equiv \int_0^1 (\tilde{A}_\theta^* \tilde{B}_\theta + \tilde{A}_z^* \tilde{B}_z) \, r \, dr. \tag{31}$$

- 53 -

For $n \neq 0$, (31) is simplified by first using the condition $\nabla \cdot \underline{B} = 0$ to eliminate $\tilde{B}_z$ through

$$r\tilde{B}_z = -\frac{1}{ik_n} \left\{ \frac{\partial}{\partial r} (r\tilde{B}_r) + im \tilde{B}_\theta \right\},$$

and then eliminating A through the relationship

$$\tilde{B}^*_r = -\frac{im}{r} \tilde{A}^*_z + ik_n \tilde{A}_\theta^*.$$

The result is

$$K_{mn} = \int_0^1 \frac{1}{ik_n} (\tilde{B}_\theta \tilde{B}^*_r - \tilde{B}^*_\theta \tilde{B}_r) r \, dr.$$

For $n = 0$, $m \neq 0$, (31) is simplified in a similar way using

$$\tilde{B}_\theta = -\frac{1}{im} \frac{\partial}{\partial r} (r\tilde{B}_r)$$

to give

$$K_{mn} = \int_0^1 \frac{r}{im} (\tilde{B}_r \tilde{B}^*_z - \tilde{B}^*_r \tilde{B}_z) r \, dr.$$

For $m = 0$, $n = 0$ (31) is simplified using the relations

$$\tilde{A}_z = \int_r^1 \tilde{B}_\theta \, dr \qquad (\text{satisfying } \tilde{A}_z = 0 \text{ at } r = 1)$$

$$\tilde{A}_\theta = \frac{1}{r} \int_0^r r\tilde{B}_z \, dr$$

to give

$$K_{00} = 2 \int_0^1 \left(\int_r^1 \tilde{B}_\theta \, dr' \right) r\tilde{B}_z \, dr.$$

To complete the calculation, the abstract expressions for the K_{mn} have to be evaluated in terms of the practical Fourier coefficients of the field <u>B</u>. If f_{mn} denotes the integrands of the expressions above for the K_{mn}, (30) may be written in general form

$$K = 2\pi L \int_0^1 r \, dr \sum_m \sum_n f_{mn} \, ,$$

and the process of folding the sums onto non-negative m and n (cf. (29)) becomes

$$\sum_m f_m = f_0 + \sum_{m=1}^{[N_\theta/2]} (f_m + f_{-m}) \qquad \text{for N odd}$$

$$= f_0 + \sum_{m=1}^{[N_\theta/2]-1} (f_m + f_{-m}) + f_{N/2} \qquad \text{for N even}$$

and similarly for index n.

If the Fourier coefficients are introduced from (11) in the form

$$\tilde{B}_r = (a_r - d_r) + i(b_r + c_r)$$

$$\tilde{B}_\theta = (a_\theta - d_\theta) + i(b_\theta + c_\theta)$$

use of the sign rules (12) gives the following explicit expressions for the folded elements above. Case $n \neq 0$:

$$f_{mn} + f_{-mn} = \frac{4}{k_n} (b_\theta a_r - c_\theta d_r - a_\theta b_r + d_\theta c_r)$$

$$f_{N_\theta/2,n} = \frac{2}{k_n} (b_\theta a_r - a_\theta b_r) \qquad (N_\theta \text{ even})$$

Case $n = 0$, $m \neq 0$:

$$f_{mn} + f_{-m,n} = \frac{4r}{m} (c_r a_z - a_r c_z).$$

Folding the elements in n merely doubles these results.

5. Program optimization and testing

The code (some 30,000 lines over all) has been written to the Fortran 77 standard and has been run on several different computers. The calculations described here used CRAY-1 and CRAY X-MP machines with an assembly language FFT package. The code has also been benchmarked on the CRAY-2.

Execution efficiency, an important requirement for practical 3-dimensional calculations, has been a primary programming consideration. In particular, it has been ensured that important loops are fully vectorized over long vectors with no memory bank conflicts.

A good vector length has been achieved by storing the data in the order (θ, z, r) and vectorizing over $\{\theta\} \times \{z\}$, $(N_\theta + 2)(N_z + 2)$ points. This approach follows naturally from the use of spectral methods in θ and z, which serves to decouple these directions from r. For instance, the tridiagonal equations for p and $\underline{B}^*$ contain m and k only as parameters. In order to allow complete vectorization of these systems, the special cases (boundary conditions etc.) have been formulated as trivial equations e.g. (22) and (26).

A second example of vectorization is the calculation of products of the form $im\tilde{B}$ (with diagram $[-mB \quad mA]$) arising from differentiation. Using an $(N_\theta + 2)(N_z + 2)$ array of signed m values in the sense $[m \quad -m]$, the required operation is simply a vectorized element-by-element multiplication of the Fourier coefficients $[A \quad B]$, followed by an interchange.

A third example of vectorization is that of interchanging and transposing θ, z values when stored in the order (θ, z, r). For the present case in which N_r usually satisfies $N_r > N_\theta$, N_z, this is done most efficiently on the CRAY machines (which allow arbitrary fixed strides through memory) by vectorizing over r rather than θ. For instance on the X-MP, when $N_\theta = 15$, $N_z = 15$, $N_r = 64$, a $\theta - z$ transpose takes 1.12 ms (33 Mflops equivalent) when vectorized over θ, but only 0.45 ms (82 Mflops equivalent) when vectorized over r. For $N_r = 128$, the times are 2.27 ms

(33 Mflops equivalent) and 0.77 ms (96 Mflops equivalent) respectively.

Typical timings for the code are given below:

mesh size $N_r \times N_\theta \times N_z$	CRAY memory words (Mwords)	CRAY-XMP CPU time/step (seconds)
$32 \times 15 \times 15$	0.27	0.21
$64 \times 12 \times 25$	0.66	0.57

A flowtrace analysis shows that 33% of the CPU time is spent in the FFT package, 65% in the numerical Fortran code and 2% in graphics.

The validation of scientific research codes is a subject rarely discussed, surely a significant omission considering their great complexity and diversity. In the view of the present author it is compounded by the rather poor level of presentation that has become common in this field, to the extent that, for instance, the omission of the offending region from the published results is sometimes perceived as an acceptable resolution of numerical problems around the origin.

Validation should be seen as important for two reasons. First, it increases the probability that the code does what is intended; there is no avoiding the fact that significant errors in large Fortran programs are

not uncommon, even in production versions. Secondly, it is essential if
the results from the code are to be received as credible by outside
observers. Unlike analytic calculations, numerical calculations
(involving so much more than the basic equations) are largely unamenable
to independent checking.

The following is an outline of the tests applied to the component modules
of the code.

Using compiler options, the code has been checked for the common
programming errors of out-of-range array indexing, the use of
un-initialized variables and mismatched subroutine argument lists.

Each module has been tested on artificial data and numerical results
confirmed by comparison with the analytic result for that operation.   The
appropriate scaling of error norm with mesh size (in particular $1/N^2$ in
radius) has been verified.

An extensive check on the advancement of $\underline{B}$ has been carried out, based on
the use of implicit and explicit treatments of resistivity. If, using the
code to calculate $\underline{B}^{n+1}$ from $\underline{B}^*$ in (6), $\underline{v}$ is set to zero, Δt is set to some
arbitrary negative value $-\Delta\tau$ and some arbitrary values used for $\underline{B}^*$ (say
$\underline{B}_0$), the result is

$$\underline{B}^{n+1} = \underline{B}_0 + \Delta\tau \, \nabla \times \left(\frac{\eta}{S} \, \nabla \times \underline{B}_0\right).$$

If this $\underline{B}^{n+1}$ is then used in the source term in the implicit calculation
of $\underline{B}^*$ in (24) and Δt set to $+\Delta\tau$, the equation to be solved is

$$\underline{B}^* + \Delta\tau \, \nabla \times \left(\frac{\eta}{S} \, \nabla \times \underline{B}^*\right) = \underline{B}_0 + \Delta\tau \, \nabla \times \left(\frac{\eta}{S} \, \nabla \times \underline{B}_0\right)$$

with trivial solution $\underline{B}^* = \underline{B}_0$. This is a thorough test since it includes the treatment of the boundary and the centre and the consistency of the 1st and 2nd steps of the numerical scheme.

As described below, testing of the code as a whole has been done using several test problems with known solutions.

6.   Typical simulations

This section contains the following examples of MHD simulation with the code:

(1)   Linear and non-linear torsional Alfvén waves.

(2)   Linear instability with uniform B_z and j_z.

(3)   Linear instability with parabolic j_z.

(4)   Linear m = 1 cylindrical tokamak tearing mode with parabolic q.

(5)   Field reversal in the pinch.

The first 4 of these constitute test problems since the results are known exactly or numerically with high precision.

6.1   Torsional Alfvén waves

The first test problem is that of torsional Alfvén waves [43], [44]. Solutions of (1) and (4) for m = 0, $\eta = 1$ and zero viscosity are sought in the form

$$\underline{v} = (0, \quad v_\theta(r,z,t), \quad 0)$$

$$\underline{B} = (0, \quad B_\theta(r,z,t), \quad 1).$$

The governing equations are

$$\frac{\partial B_\theta}{\partial t} = \frac{\partial}{\partial z}\left\{v_\theta B_z + \frac{\eta}{S}\frac{\partial B_\theta}{\partial z}\right\} + \frac{\partial}{\partial r}\left\{\frac{\eta}{S}\frac{1}{r}\frac{\partial}{\partial r}(rB_\theta)\right\}$$

$$\frac{\partial v_\theta}{\partial t} = B_z \frac{\partial B_\theta}{\partial z}$$

with exact arbitrary amplitude solution

$$B_\theta = J_1(\lambda r) \exp i(kz + \omega t)$$

$$v_\theta = (k/\omega) J_1(\lambda r) \exp i(kz + \omega t)$$

in which

$$\lambda^2 \equiv \frac{iS}{\eta}(-\omega + k^2/\omega) - k^2$$

and

$$J_0(\lambda) = 0,$$

corresponding to the boundary condition $E_z = 0$.

As a simple diagnostic, the mean B_θ and v_θ in a given z plane have been computed through

$$\langle B_\theta \rangle = \frac{1}{\pi} \int_0^{2\pi} \int_0^1 B_\theta \, r \, dr \, d\theta.$$

The real and imaginary parts of the frequency (ω_r and ω_i) are calculated by assuming a form

$$\langle B_\theta(t) \rangle = \langle B_\theta(0) \rangle \exp(-\omega_i t) \exp i \, (\omega_r t + kz)$$

and then performing a non-linear least squares fit to the numerical results.

Fig. 6 shows the results for the case $S = 10^3$, $L = 3$, $n = 1$ for $N_r = 32$. Here $\langle B_\theta \rangle$ is plotted vs. time for a small amplitude wave, using the exact eigenfunction as the initial condition. The analytic solution is also shown (dashed line) and demonstrates the presence of numerical dissipation in the simulation.

Fig. 7 shows ω_r and ω_i vs. timestep. The damping rate shows the linear dependence on timestep expected from the theoretical expression (9). The analytic values of ω_r and ω_i are 2.094389 and 5.080 10^{-3}. In the limit $\Delta t \to 0$ the simulation values are accurate to 0.005% and 12% respectively.

This problem also provides an exact non-linear test of the code and furnishes a particularly clear demonstration of the effect of aliasing error on non-linear simulations.

Fig. 8 shows $\log_{10}$ of the energy spectrum of v_θ plotted vs. time when all field amplitudes are O(1) and there is no de-aliasing in z. In this case the simulation fails, $\underline{v}$ and $\underline{B}$ suddenly tending to infinity. Fig. 9 shows the corresponding radial eigenfunctions with the alternating spikes characteristic of numerical instability.

This behaviour is an example of the non-linear explosive instability discussed in section 3.10, arising from the aliasing error in z. (In this example - an exact non-linear solution with fixed k - the aliasing error occurs because of a cascade of numerical errors to high k. However, this is no different in its effect from a cascade of physical energy, as would generally be the case).

The detailed behaviour of this numerical instability may be understood from the analysis given in [38], which predicts the explosive time dependence B, v $\sim$ $1/(t_c - t)$ in which t_c is an undetermined characteristic singular time. It follows from this theory that log plots of kinetic energy, magnetic energy and timestep ($\propto 1/B$ from the Courant timestep condition) against $-\log(t_c - t)$ should have gradients +2, +2 and -1 respectively. (In practice, t_c is taken to be the final time in the calculation and to preserve numerical accuracy, $t_c - t$ is computed by accumulating the values of the timestep backwards from the end of the calculation). Fig. 10 shows such plots for the present calculation, with the theoretical scaling lines (dashed). There is clearly very good agreement between the observed and predicted numerical behaviour.

In contrast, Fig. 11 shows the energy spectrum plot of the successful simulation obtained when the same calculation is de-aliased in z according

to (27). (The m=0, n=3 mode is present as numerical error). Fig. 12
shows the corresponding radial eigenfunction for B_θ, indistinguishable
from the analytic profile.

6.2 Linear instability with uniform B_z and j_z

The linear instability with a uniform B_z and j_z is another useful test of
the code on the Alfvén timescale. The problem has most recently been
discussed by Storer [45].

The equilibrium fields for this problem may be written

$$\underline{v}_0 = 0$$

$$B_r = 0$$

$$B_\theta = rj_z/2 = (2\pi/L)(r/q)$$

$$B_z = 1$$

$$E_z = (\eta/S)j_z$$

in which $\eta = 1$ and q is a constant.

The linear eigenfunctions given in [45] may be written

$$b_r = - \left[\frac{m}{\lambda^2 r} (\alpha + k) J_m(\lambda r) - \frac{k}{\lambda} J_{m-1}(\lambda r) \right] \sin(m\theta - kz) e^{\gamma t}$$

$$b_\theta = \left[\frac{m}{\lambda^2 r} (\alpha + k) J_m(\lambda r) - \frac{\alpha}{\lambda} J_{m-1}(\lambda r) \right] \cos(m\theta - kz) e^{\gamma t}$$

$$b_z = J_m(\lambda r) \cos(m\theta - kz) e^{\gamma t}$$

in which

$$\alpha^2 \equiv \lambda^2 + k^2.$$

The eigenvalue λ is fixed by the boundary condition $b_r = 0$ and is a solution of

$$(k \pm |\alpha|) \, m \, J_m(\lambda) - k\lambda \, J_{m-1}(\lambda) = 0.$$

The growth rate γ is then determined from

$$\gamma = \frac{-\eta\alpha^2}{2S} + \left[\left(\frac{\eta\alpha^2}{2S}\right)^2 - \left(\frac{B_\theta}{r}\right)^2 \left\{ (m - nq)^2 + 2(m - nq)\frac{k}{\alpha} \right\} \right]^{1/2}.$$

The real part of the frequency is zero for an unstable mode.

The values used for the simulation were $L = 3$, $m = 2$, $n = 1$, $q = 1.4$, $S = 10^3$, with analytic results $\lambda = 4.291575$, $\alpha = -4.775365$ and growth rate $\gamma = 0.598770$. Only the fundamental eigenfunction is unstable for this choice of parameters.

Fig. 13 shows a plot of $\log_{10}$ of the $m = 2$ energy spectrum value of v_θ vs. time, starting from a small perturbation but not the eigenfunction. The mode grows exponentially until non-linear effects become important. The linear growth rate is accurate to 1%. Fig. 14 shows a comparison of the simulation radial eigenfunction and the analytic profile.

Note that the analytic solution given above and the corresponding simulation described here are not absolutely identical, owing to a slight difference in the boundary conditions (the analytic solution has a non-zero perturbation current at the wall whereas the simulation does not). For a strongly unstable global mode, this difference should have only a small local effect and no doubt accounts for the slight difference in the analytic and simulation profiles apparent at the wall.

6.3   Linear instability with parabolic j_z

Another more general test of the code on linear problems is provided by the instabilities in the equilibrium

$$B_r = 0$$
$$B_\theta = \text{const.} \ (r/2 - r^3/4)$$
$$B_z = 1$$

i.e. a uniform B_z and parabolic j_z.

Fig. 15(a) shows $\log_{10}$ of the energy spectrum of v_θ vs. time, starting from a seed of white noise for the case $L = 3$, const. $= 8$, $S = 10^3$ with $N_r = 64$, $N_\theta = 15$, $N_z = 15$. The decay of the damped modes and the exponential growth of the unstable modes can be clearly seen. Fig.15(b) gives another representation of these results.

The exact linear growth rates for this problem are not known analytically, but have been found numerically to great precision using a resistive MHD

eigenvalue solver. Since the boundary condition $j_r = 0$ used in the eigenvalue solver does not obtain in the present code, the comparison cannot be exact. However, for the fast global modes being studied here, any discrepancy should be rather small.

The following table shows the comparison between the values of simulation growth rate (lower values) and eigenvalue (upper values) for the different unstable modes in the simulation.

	m = 0	m = 1	m = 2	m = 3
n = 2	1.383			
	1.285			
n = 1	1.289			
	1.297			
n = -1		1.912		
		1.904		
n = -2		1.090	2.048	
		1.152	2.060	
n = -3		2.159	2.035	1.545
		2.150	1.942	1.586
n = -4		1.598	1.717	2.354
		1.393	1.759	2.331
n = -5			2.311	1.818
			2.274	1.261
n = -6			1.281	2.032
			0.739	2.066
n = -7				2.269
				2.180

It can be seen that these sets of results are generally in good agreement.

6.4   Linear m = 1 cylindrical tokamak tearing mode with parabolic q

This problem provides a test of the code on a long timescale on a problem with a narrow resistive layer.   The equilibrium fields are

$$B_r = 0$$

$$B_\theta = \frac{j_0 r/2}{1 + (r/r_c)^2}$$

$$B_z = 1$$

in which j_0 is a parameter, related to q by

$$q(0) = 2/j_0 R$$

in which R is the major radius ($L/2\pi$). This is the 'peaked' profile introduced for the analytic study of tearing modes [46] and subsequently used for numerical simulations [47].

As is usual in such calculations a resistivity profile $\eta(r)j_z(r) = $ const. is used to maintain the equilibrium current against ordinary resistive diffusion.   Here, the constant is determined by fixing the value $\eta = 1$ at the resonant surface.

The values used in the simulation were: m = 1, n = -1, $r_c = 0.6$, q(0) = 0.9 and hence q(1) = 3.4 and the position of the resonant surface $r_s = 0.2$.

The aspect ratio was taken as 10 (L = 20π) and S was a parameter, varied in the range $10^4 \rightarrow 10^8$.

A complication of the present simulation is the presence of the ideal m = 1 internal mode, always unstable in a cylinder if there is a q = 1 surface in the plasma, with growth rate scaling as

$$\gamma \approx B_z \frac{q^2}{|q'|} \frac{1}{R^3} O(1)$$

for large aspect ratio. Since the growth rate of the resistive mode scales less strongly, the relative importance of the two modes may be selected by choosing an appropriate aspect ratio. The value R = 10 used here is such that the ideal growth rate is not negligible. This is reflected in the results for the growth rate γ at large S.

Fig. 16 shows a plot of $\log_{10}\gamma$ vs. $\log_{10}S$ obtained for this simulation. The solid line is the exact result, computed numerically using the resistive eigenvalue solver discussed in the previous section, and the individual points are the simulation results. It can be seen that there is excellent agreement. Fig. 17 shows the characteristic shape of the eigenfunction for the case S = 10^6.

Given the example of the torsional Alfvén wave (section 6.1), in which numerical dissipation ("numerical resistivity") dominated the calculation at even a modest S (10^3), it is natural to ask how the code can give such accurate values for the tearing mode growth rate at S = 10^8. This can be answered using expression (9), relating the physical and numerical growth

rates and the effects of time discretization. For the growing tearing

mode studied here, $\omega_r = 0$ so that in (9)

$$(\omega_r)_{num} \simeq 0$$

$$\gamma_{num} \simeq \gamma - \frac{1}{2}\gamma^2 \Delta t.$$

(Here, negative γ implies growth). Since $|\gamma \Delta t| \ll 1$ by hypothesis (and

typically 10^{-2} in practice), this indicates that the numerical growth rate

should be close to the true growth rate (and marginally larger), as

observed. This would not generally be the case if the mode had a complex

growth rate.

6.5   Field Reversal in the Pinch

This section mentions briefly how the code has been applied to the

simulation of field reversal in the Reversed Field Pinch [3]. A full

discussion of this work and its comparison with experiment may be found in

[2].

The object of the calculation is to simulate and subsequently analyze the

dynamics of the field reversal phenomenon, that is the spontaneous

generation of internal currents such that the magnetic field B_z assumes a

radially decreasing profile and becomes negative at the wall. Although

the nature of the final reversed state is described by relaxation theory

[41], the nature of the detailed mechanism is not similarly available.

Investigation by numerical simulation is then particularly relevant for

not only is the process inherently non-linear, but also is apparently very robust.

Of particular recent interest is the study of the maintenance of field reversal in the initial force-free reversed state defined by [7]

$$q(r) = 0.4 (1.0 - 1.8748r^2 + 0.83232 r^4)$$

for the case $\eta = 1$, $S = 10^3$, $L = 2\pi$ (unit aspect ratio). In the present calculations the initial state is seeded with white noise at a relative amplitude of 10^{-6} and the code run with $E_\theta = 0$ and $E_z = $ const. for some substantial fraction of a field diffusion time. The value of E_z is chosen to give an appropriate value of total current in the final state.

The magnitude of reversal is conventionally measured by the quantity F, defined as the average value of B_z at the wall, normalized to its average over the volume.

Fig. 18 shows a typical plot of F vs. time for a run with numerical parameters $\nu = 10^{-4}$, $E_z = 1.771 \; 10^{-3}$, $N_r = 32$, $N_\theta = 12$, $N_z = 25$ (i.e. mode numbers $0 \leqslant m \leqslant 3$, $-8 \leqslant n \leqslant 8$ are included). As the simulation proceeds the field rapidly loses the reversal of the initial state, but then suddenly reverses and remains marginally reversed for the rest of the calculation, although with slight fluctuations. For comparison, the dashed line shows how it would evolve (under axisymmetric resistive diffusion) if there were no non-linear terms in the equations.

Since there is no a-priori reason for field reversal to be produced by an MHD model, the implication of such numerical modelling is that a classical single-fluid dynamo theory may be sufficient to explain this remarkable phenomenon.

Acknowledgement

References

1. H.A.B.Bodin, B.E.Keen, Reports on Progress in Physics 40, 95 (1977).

2. P.Kirby, Culham Laboratory Preprint CLM-P 803 (1987) submitted to Phys. Fluids.

3. H.A.B.Bodin, A.A.Newton, Nuclear Fusion 20, 1255 (1980).

4. P.Kirby, Culham Laboratory Preprint CLM-P 809 (1987) submitted to Nuclear Fusion.

5. A.W.Edwards, D.J.Campbell, W.W.Engelhardt, H.-U. Fahrbach, R.D.Gill, R.S.Granetz, S.Tsuji, B.J.D.Tubbing, A.Weller, J.Wesson, D.Zasche, Phys. Rev. Lett. 57, 210 (1986).

6. J.P.Freidberg, Rev. Mod. Phys. 54, 801 (1982).

7. A.Y.Aydemir, D.C.Barnes, E.J.Caramana, A.A.Mirin, R.A.Nebel, D.D.Schnack, A.G.Sgro, Phys. Fluids 28, 898 (1985).

8. Y.Tanaka, M.Azumi, G.Kurita, T.Takeda, Plasma Physics and Controlled Fusion 27, 579 (1985).

9. D.S.Harned, W.Kerner, J. Comp. Phys. 60, 62 (1985).

10. D.S.Harned, D.D.Schnack, J. Comp. Phys. 65, 57 (1986).

11. D.S.Harned, W.Kerner, Nuc. Science and Engineering 92, 119 (1986).

12. D.S.Harned, Courant Institute of Mathematical Sciences Report DOE/ER/53223-18(1986).

13. A.J.Robert, Proc. WMO/IUGG Symposium on Numerical Weather Prediction, Tokyo, 1969.

14. S.A.Orszag, A.T.Patera, Phys. Rev. Lett. 47, 832 (1981).

15. D.D.Schnack, D.C.Baxter, E.J.Caramana, J. Comp. Phys. 55, 485 (1984).

16. K.V.Roberts, J.P.Boris, Proc. Culham Conference on Computational Physics Vol.2 paper 44 (1969).

17. J.Killeen, Proc. 10th IFIP Conference on System Modelling and Optimization (1981); Lawrence Livermore Laboratory Preprint UCRL-85440 (1981).

18. A.Sykes, J.A.Wesson, Proc. 8th European Conference on Controlled Fusion and Plasma Physics, Prague, Vol.1, p.80 (1977).

19. A.Sykes, J.A.Wesson, Phys. Rev. Lett. 37, 140 (1976).

20. A.Y.Aydemir, D.C.Barnes, J. Comp. Phys. 53 100 (1984).

21. J.P.Dahlburg, D.Montgomery, G.D.Doolen, L.Turner, Phys. Rev. Lett. 57, 428 (1986).

22. D.D.Schnack, D.C.Barnes, Z.Mikic, D.S.Harned, E.J.Caramana, S.A.I.C. Report 86/3022--APPAT-83 (1986). (To appear in J. Comp. Phys.).

23. L.A.Charlton, B.A.Carreras, R.J.Hastie, T.C.Hender, J.A.Holmes, V.E.Lynch, Bull. Am. Phys. Soc. paper 7P2 (November 1986).

24. D.Biskamp, H.Welter, Proc. 11th International Conference on Plasma Physics and Controlled Nuclear Fusion Research, Kyoto, paper CN-47/E-I-1-2 (1986).

25. R.J.Bickerton, Proc. Phys. Soc. 72, 618 (1958).

26. S.A.Orszag, J. Fluid Mech. 49, 75 (1971).

27. S.A.Orszag, Studies in Applied Math. 50, 293 (1971).

28. A.Arakawa, J. Comp. Phys. 1, 119 (1966).

29. C.H.Finan III, J.Killeen, Computer Physics Communications 24, 441 (1981).

30. F.H.Harlow, J.E.Welch, Phys. Fluids 8, 2182 (1965).

31. E.A.Dorfi, Computer Physics Communications 43, 1 (1986).

32. P.J.Roache, 'Computational Fluid Dynamics', Hermosa Publishers (1976).

33. I.Yu.Brailóvskaya, Soviet Physics Doklady 10, 107 (1965).

34. B.V.Waddell, M.N.Rosenbluth, D.A.Monticello, R.B.White, B.Carreras, 'Theoretical and Computational Plasma Physics' Trieste (1977), IAEA Vienna (1978) p.79.

35. C.Temperton, J. Comp. Phys. 52, 340 (1983).

36. G.P.Williams, J. Fluid Mech. 37, 727 (1969).

37. R.Peyret, T.D.Taylor, 'Computational Methods for Fluid Flow', Springer Verlag (1983) p.164.

38. J.W.Eastwood, W.Arter, Phys. Rev. Lett. 57, 2528 (1986).

39. P.J.Davies, P.Rabinowitz, 'Methods of Numerical Integration', Academic Press (1975) p.106.

40. H.Engels, 'Numerical Quadrature and Cubature', Academic Press (1980) p.23.

41. J.B.Taylor, Rev. Mod. Phys. 58, 741 (1986).

42. M.K.Bevir, private communication (August 1983).

43. S.Lundquist, Phys. Rev. 76, 1805 (1949).

44. D.F.Jephcott, P.M.Stocker, J. Fluid Mech. 13, 587 (1962).

45. R.G.Storer, Plasma Physics 25, 1279 (1983).

46. H.P.Furth, P.H.Rutherford, H.Selberg, Phys. Fluids 16, 1054 (1973).

47. B.V.Waddell, M.N.Rosenbluth, D.A.Monticello, R.B.White, Nuclear Fusion 16, 528 (1976).
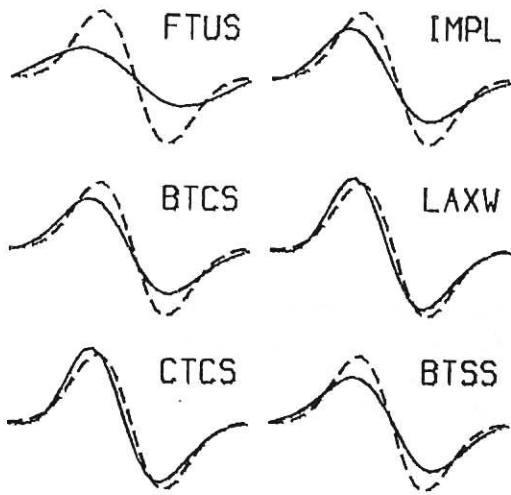
1. Illustrative one-dimensional linear advection tests: forward-time upwind-space (FTUS), fully implicit (IMPL), Brailovskaya-time centred-space (BTCS), Lax-Wendroff (LAXW), centred-time centred-space (CTCS), Brailovskaya-time spectral-space (BTSS). Mesh size$=32$, $v\Delta t/\Delta x=0.25$. The dashed line shows the exact result.

N=4

f_4	f_1	f_2	f_3	f_4	f_1

N=5

f_5	f_1	f_2	f_3	f_4	f_5	f_1
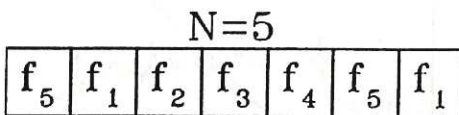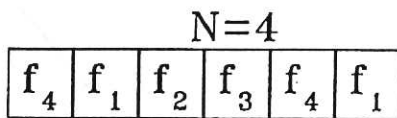
2(a) Example layout of grid values of a periodic function f for even and odd N. The periodicity is made explicit.

N=4

A_0	B_0	A_1	B_1	A_2	B_2

N=5

A_0	B_0	A_1	B_1	A_2	B_2	
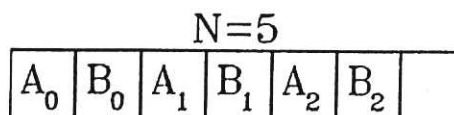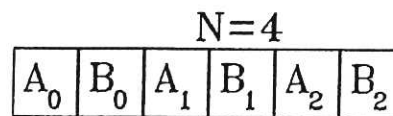
2(b) Layout of complex Fourier coefficients corresponding to fig.2(a).

3. Layout of quantities on the staggered radial mesh. 0=even mesh points, x=odd mesh points. (For convenience, only 2 radial points are shown and the lists of items have been split in two).

r=0	$N_r=2$		r=1
B_θ	B_r	$v\times B_r$	$j\times B_r$
B_z	v_r	E_r	$v\cdot\nabla v_r$
v_θ	j_θ	$j\times B_\theta$	ω_θ
v_z	j_z	$j\times B_z$	ω_z
p	$v\times B_\theta$	$v\cdot\nabla v_\theta$	
$\nabla\cdot B$	$v\times B_z$	$v\cdot\nabla v_z$	
j_r	E_θ	ω_r	
	E_z		
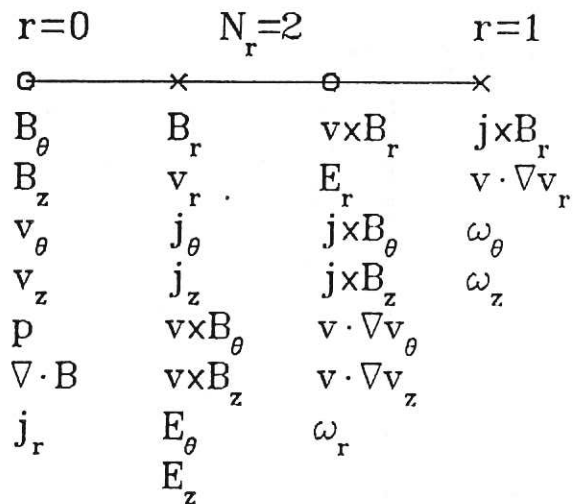
r=0　　　　N_r=10　　　r=1

o—o—o—o—o—o—o—o—o—o—x

$\dfrac{3}{8}$　$\dfrac{9}{8}$　$\dfrac{9}{8}$　$\dfrac{17}{24}$　$\dfrac{4}{3}$　$\dfrac{2}{3}$　$\dfrac{4}{3}$　$\dfrac{3}{4}$　$\dfrac{25}{24}$　$\dfrac{25}{24}$

r=0　　　　N_r=9　　　r=1

o—o—o—o—o—o—o—o—o—x

$\dfrac{1}{3}$　$\dfrac{4}{3}$　$\dfrac{2}{3}$　$\dfrac{4}{3}$　$\dfrac{2}{3}$　$\dfrac{4}{3}$　$\dfrac{3}{4}$　$\dfrac{25}{24}$　$\dfrac{25}{24}$

4. Example layout of radial integration coefficients for even mesh points for odd and even N_r. Coefficients for odd mesh points are the same but in reverse order.

5. Typical plots of $\nabla.v$ and $\nabla.B$ vs. time. $\nabla.B$ rises steadily as a result of rounding error. $\nabla.v$ is maintained at a low level by the pressure correction.
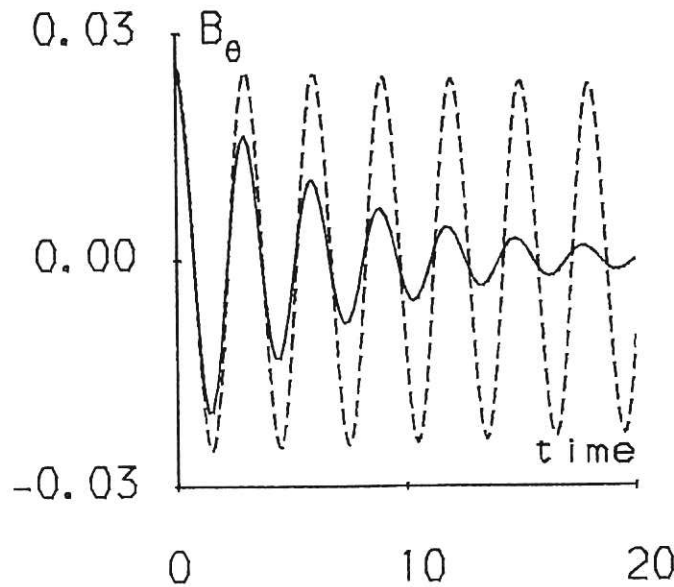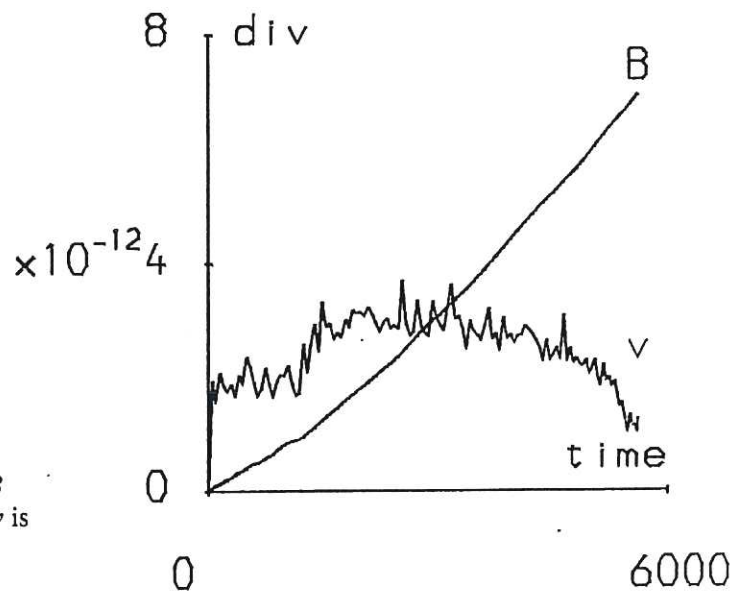
6. Mean B_θ vs. time for the simulation of a linear torsional Alfvén wave. Comparison of the simulation result (solid line) with the analytic result (dashed line) demonstrates the presence of numerical dissipation.
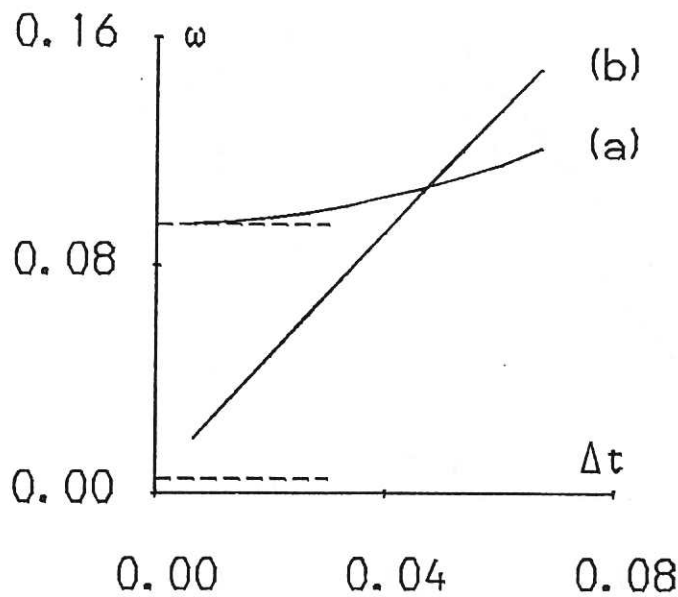
7. Frequency ω vs. timestep for the simulation of fig.6. (a) is
$Re(\omega)-2$, (b) is $Im(\omega)$. The dashed lines show the analytic values.
As expected from numerical analysis, the imaginary part is
proportional to the timestep and gives the analytic value only on
extrapolation to zero timestep.
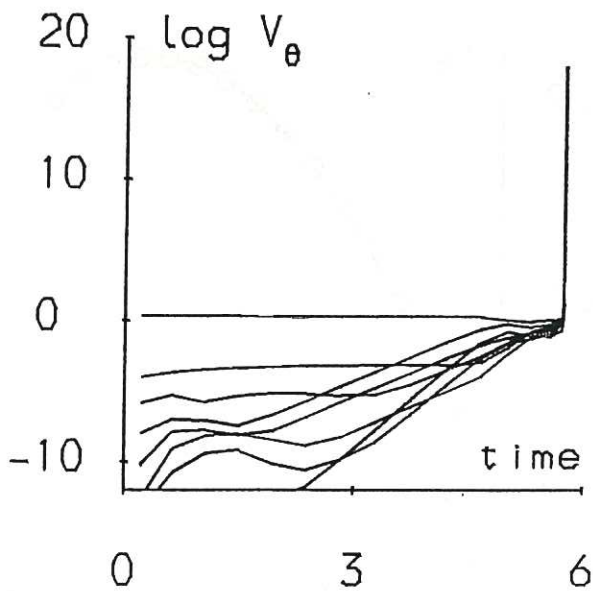
8. Log of energy spectrum of v_θ vs. time for the
aliased simulation of a non-linear torsional
Alfvén wave. Each trace shows the energy in a
particular m,n harmonic. The calculation rapidly
fails with a non-physical blow-up.
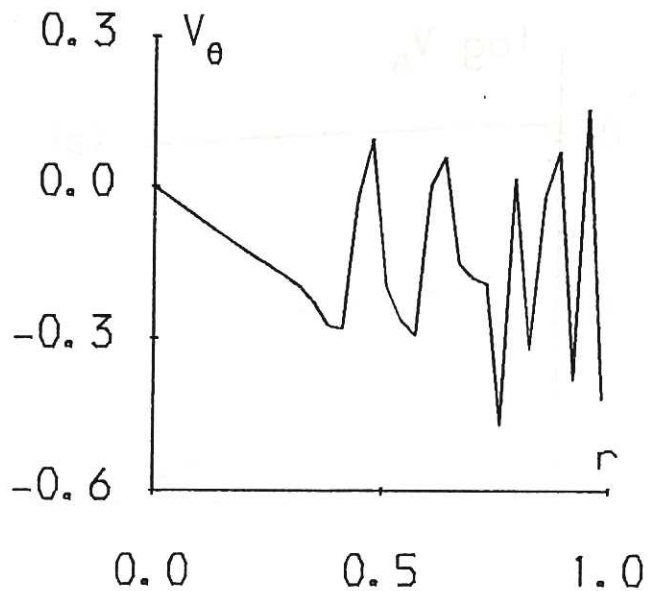
9. Radial eigenfunction of v_θ at the onset of the
blow-up of fig. 8, showing the alternating spikes
typical of numerical instability.
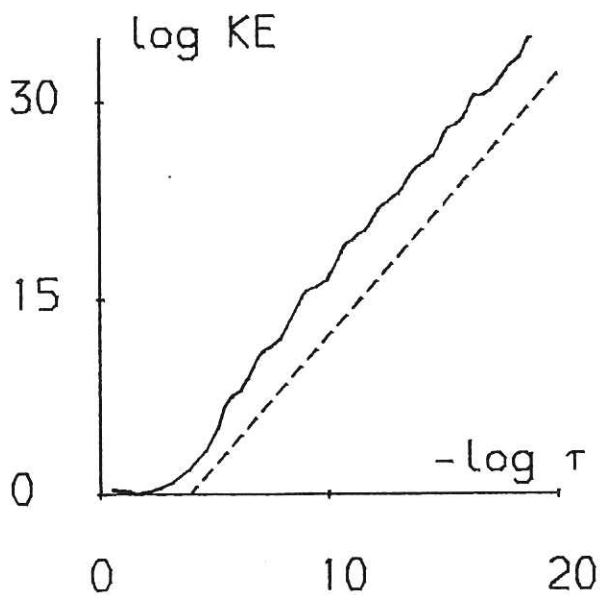
10(a) Log of total kinetic energy vs. $-\log \tau$ ($\tau \equiv t_c - t$) for the blow-up of fig.8. The dashed line shows the theoretical slope ($+2$) for a $1/t$ explosive instability.
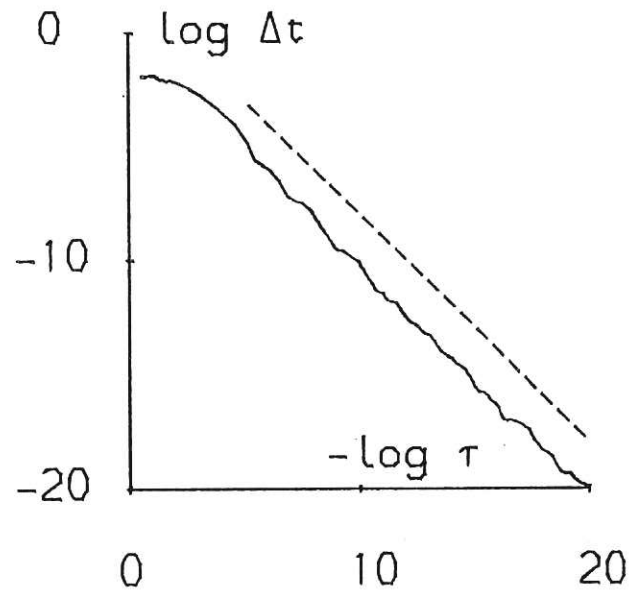
10(b) Log of timestep vs. $-\log \tau$ ($\tau \equiv t_c - t$) for the blow-up of fig.8. The dashed line shows the theoretical slope (-1) for a $1/t$ explosive instability.
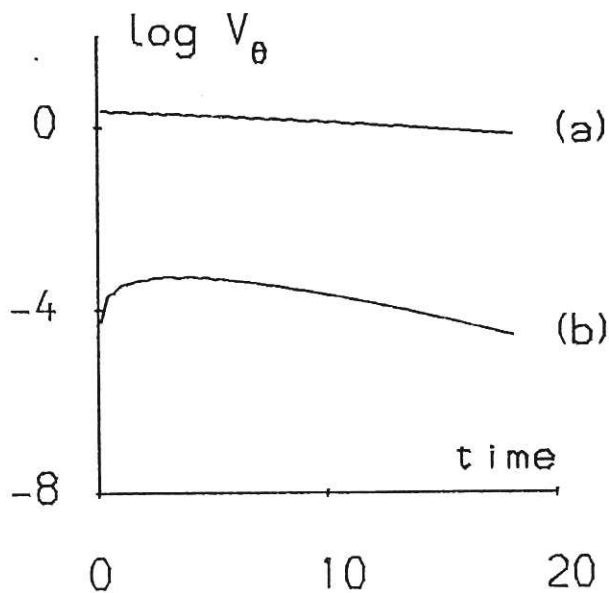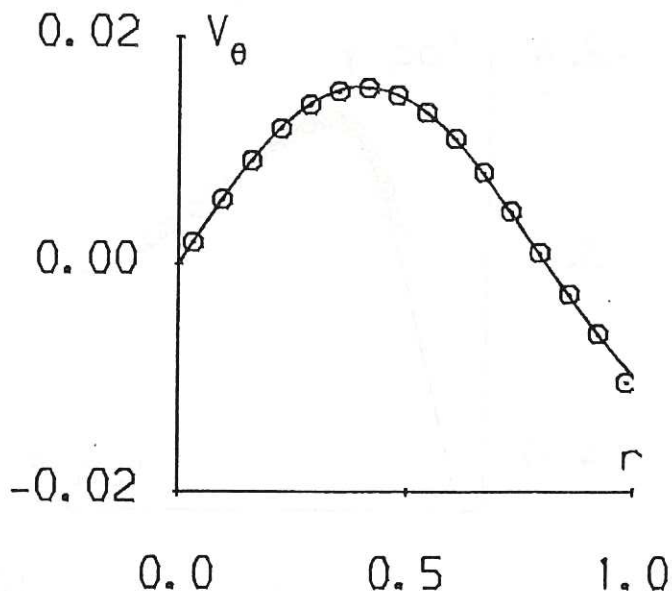
11. Log of energy spectrum of v_θ vs. time for the de-aliased simulation of a non-linear Alfvén wave. Trace (a) is the simulated $n=1$ mode and trace (b) is a small $n=3$ error field. This successful simulation is to be contrasted with that of fig.8.
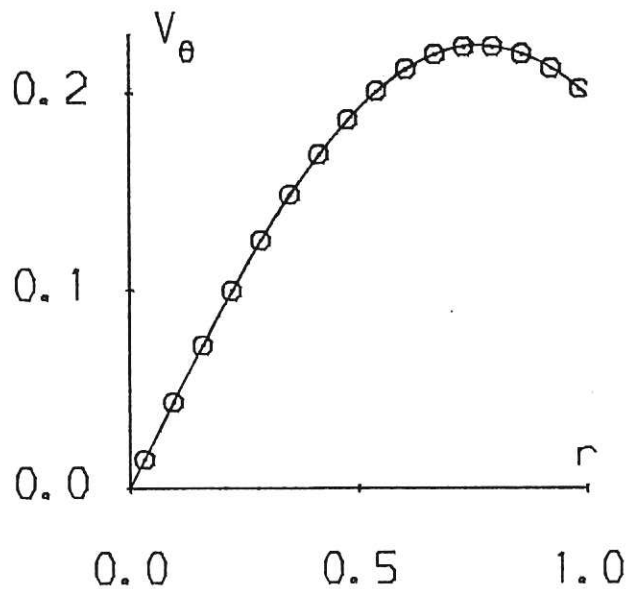
12. Radial eigenfunction of v_θ for the simulation of fig.11. The simulated shape of the eigenfunction (markers) is in good agreement with the analytic result (solid line).
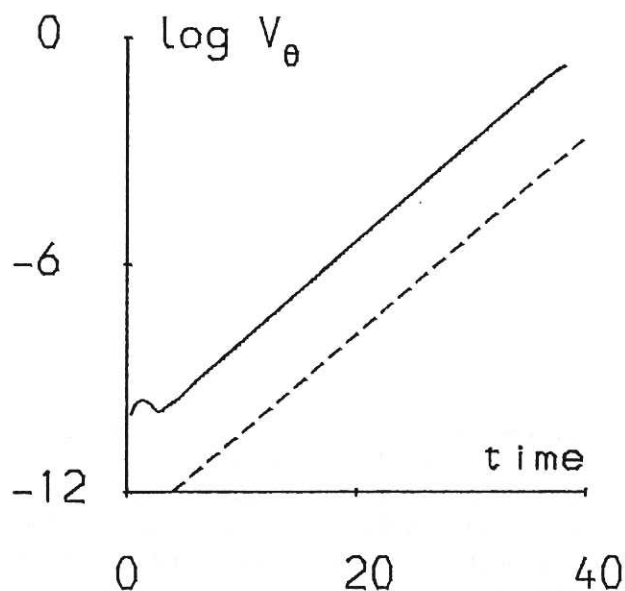
13. Log of energy spectrum of v_θ vs. time for the simulation of the linear $m=2$ instability with uniform B_z and j_z. The simulation growth rate $\gamma=0.606$. The dashed line shows the theoretical slope ($\gamma=0.599$).


14. Radial eigenfunction of v_θ for the simulation of fig. 13. The simulated shape of the eigenfunction (markers) is in good agreement with the analytic result (solid line).
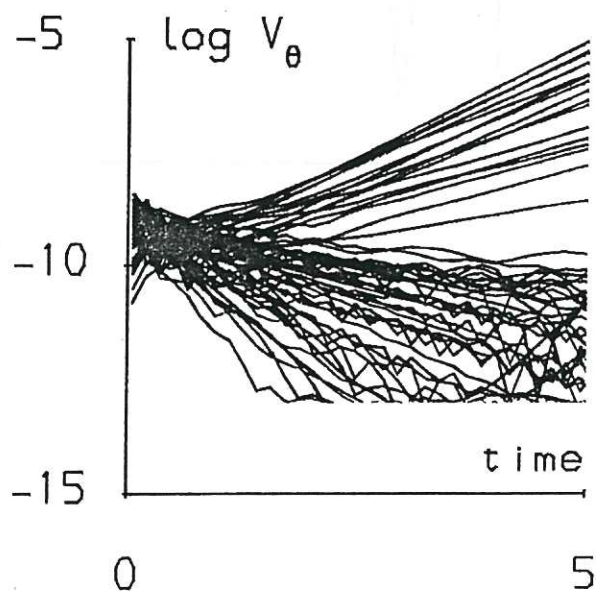

15(a) Log of energy spectrum of v_θ vs. time for the simulation of the linear instabilities with parabolic j_z. The damped and growing modes are seen to evolve from the initial white noise.
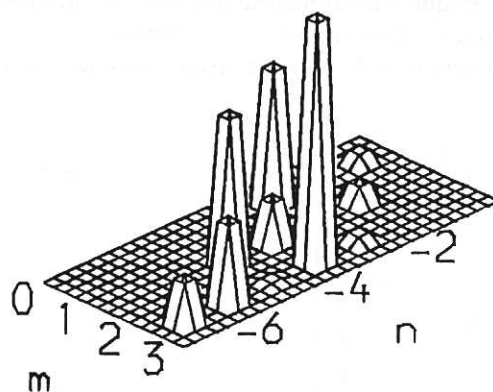

15(b) Energy spectrum of v_θ at the end of the simulation of fig. 15(a), plotted as an isometric histogram in m,n space. The band of instability and the relative amplitudes of the modes are immediately apparent from this diagnostic.
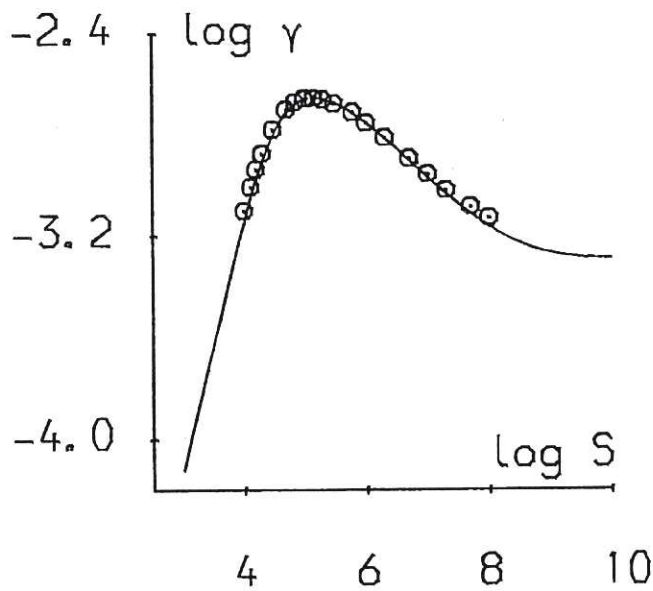
16. Log growth rate γ vs. log S for the simulation of the linear $m=1$ tokamak tearing mode. The simulation results (markers) are in good agreement with the exact results (solid line). The behaviour at large S is due to the presence of the ideal $m=1$ instability.
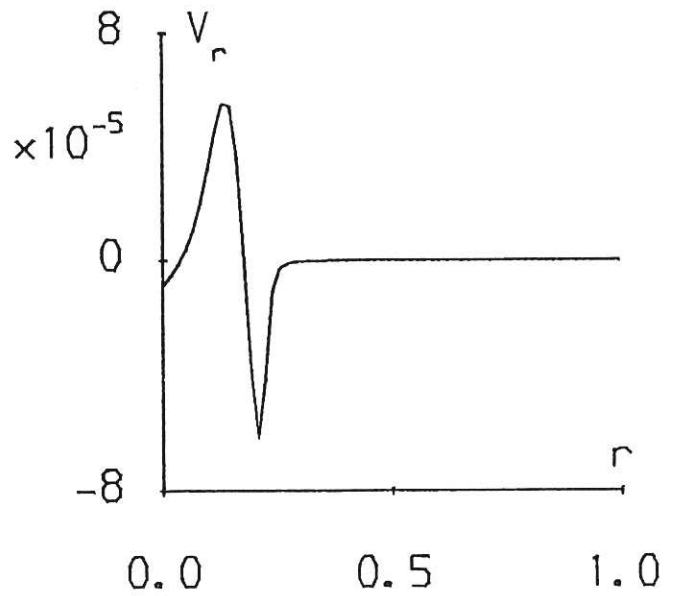
17. Radial eigenfunction of v_r for the simulation of fig. 16, showing the narrow region characteristic of resistive instabilities. ($S=10^6$).
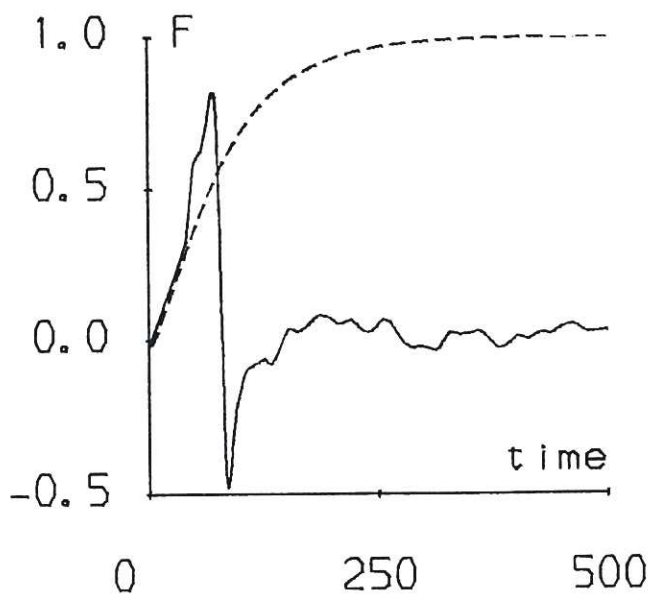
18. Field reversal fraction F vs. time for the simulation of the Reversed Field Pinch. After an initial phase, the simulation shows marginal reversal ($F=0$) with some fluctuations. For comparison, the dashed line shows how F would evolve if it were governed only by axisymmetric resistive diffusion.